Available online at www.sciencedirect.com
SCIENCE DIRECT®
Wear 257 (2004) 962–983
WEAR
www.elsevier.com/locate/wear

Contact fatigue failure evaluation of post-treated WC–NiCrBSi functionally graded thermal spray coatings

S. Stewart [a], R. Ahmed [a,*], T. Itsukaichi [b]

[a] *School of E.P.S., Heriot Watt University, Edinburgh, Scotland, UK*
[b] *Fujimi Inc., 82-28 Kakamihigashi-machi-5, Kakamigahara, Gifuken 509-0103, Japan*

Received 6 October 2003; received in revised form 23 April 2004; accepted 21 May 2004

Abstract

Functionally graded thermal spray coatings applied to industrial components, which are subjected to contact fatigue or repeated impact loading, can reduce components weight and internal stresses whilst improving the adhesive strength to combat surface and sub-surface crack propagation. However, defects within the coating microstructure, which cannot be removed by the functionally graded approach, can compromise components reliability in high stress tribological applications. Post-treatments such as vacuum heating and Hot Isostatic Pressing (HIPing) have been shown in scientific studies to improve the coating microstructure, however, the influence of post-treatment on thermal spray coatings in rolling/sliding contacts have been seldom reported.

This paper reports the rolling contact fatigue (RCF) analysis of functionally graded WC–NiCrBSi coatings deposited by a JP5000 system and subjected to post-treatment. HIPing was carried out at two different furnace temperatures of 850 and 1200 °C, whilst vacuum heating was performed at the elevated temperature of 1200 °C. The rate of heating and cooling was kept constant at 4 °C/min. RCF tests were conducted using a modified four-ball machine under various tribological conditions of contact stress and configuration, in both full film and mixed elasto-hydrodynamic lubrication (EHL).

Test results reveal that the performance of coatings was highly dependent on the changes within the coating microstructure. Coatings HIPed at 1200 °C displayed relatively improved RCF performance over the as-sprayed coatings at stress levels of 2 and 2.7 GPa in full film lubrication. Improvement in RCF performance was attributed to the densification and homogeneity within the coating microstructure.

Keywords: Rolling contact fatigue; Thermal spray coating; Post-treatment; HIPing

1. Introduction

Protective coatings on components of industrial machinery are expected to meet stringent requirements for adhesion, surface impact tolerance and wear resistance. Conventionally, coatings of this type have been deposited by a plasma-based thermal spraying process, however, methods such as high velocity oxy fuel (HVOF) thermal spraying have been shown to produce more wear resistant coatings [1]. When a material is applied in the form of a protective coating, difficulties arise due to mismatch in elastic moduli, thermal expansion coefficients and hardness between the surface layer and the base material. Such differences in material properties lead to the generation of residual (process induced) or operation related internal stresses, and may cause the coating to delaminate or form a crack network, with implications of poor component performance under high stress cyclic contact or impact loading. This limits the applications of certain hard facing materials with otherwise excellent wear characteristics.

The process of functionally grading a protective coating can successfully enhance the material's performance, while maintaining or reducing fabrication costs. Functionally graded materials (FGMs) deposited by thermal spraying have been incorporated within industry to minimise friction and wear, and also reduce the tribological requirements for the base material of coated components. Some of these ap-

Abbreviations: APS, air plasma spraying; D-Gun, detonation gun; DTA, differential thermal analysis; EDX, energy dispersive X-ray; EHL, elasto hydrodynamic lubrication; EPMA, electron probe microscopy analysis; FGM, functionally graded material; HIPing, hot isostatic pressing; HVOF, high velocity oxy-fuel; HVPS, high velocity plasma spraying; PVD, physical vapour deposition; RCF, rolling contact fatigue; RMS, root mean square; XRD, X-ray diffraction

* Corresponding author. Tel.: +44 131 451 4722; fax: +44 131 451 3129.
E-mail address: r.ahmed@hw.ac.uk (R. Ahmed).

0043-1648/$ – see front matter © 2004 Published by Elsevier B.V.
doi:10.1016/j.wear.2004.05.008

Nomenclature

N	speed of the drive shaft (rpm)
R_1	radius of the coated disc (mm)
R_2	radius of the lower planetary ball (mm)
Z	number of planetary balls

Greek letters

ω_a	angular velocity of the upper drive disc about the spindle axis MN
ω_p	angular velocity of the planetary ball about the axis MN
ω_s	spin angular velocity of the planetary ball about the axis inclined at angle β to the spindle axis MN

plications include aerospace, pulp and paper, as well as the oil and offshore industries [2–5].

Advanced bearing components such as gears, traction drives, cams and tappets contemplated for future transportation systems and advanced aircraft engines are required to operate under severe tribological and environmental constraints. High service temperatures, extreme contact pressures, marginal lubrication and harsh environmental conditions are some of the concerns that require improved tribological designs, high performance bearing materials, and effective lubrication methods. This drives the development and implementation of post-treated protective coatings since thermal spray coatings not only have significant porosity but also secondary phase particles and a lack of fusion which will not be removed by the FGM approach [6].

HIPing and vacuum heating are two types of post-treatments adapted for this investigation. Vacuum heating is a conventional heat treatment process, which has a significant influence on the tribological performance of HVOF coatings [7,8]. At elevated temperatures, the effective carbide content of the coating is increased through recrystallization of the amorphous phase into eta-carbides, which improves wear resistance [9]. Hot Isostatic Pressing (HIPing) combines both high temperature and pressure to improve the coating microstructure. At high temperatures of HIPing, interlamellar porosity is completely eliminated while spherical pores, approximately 2 μm in diameter are reduced to micro-voids less then 0.1 μm in size [10].

Prior to this investigation, the rolling contact fatigue performance of post-treated functional graded thermal spray coatings was assessed using a modified four-ball rolling machine [11]. Results revealed that the relative performance of the coating was highly dependent on the changes within the coating microstructure. Under a Hertzian contact stress of 2 GPa and in full film lubrication, coatings HIPed at 1200 °C displayed significant improvement in relative performance over the as-sprayed coatings, however, at higher magnitudes of contact stress, it was difficult to ascertain the potential improvement in RCF performance of the post-treated coatings. This was due to relatively high degree of sliding within the contact region, which led to asperity interaction during RCF testing. In the following analysis, the configuration of the modified four-ball machine was changed by replacing the three lower planetary balls with a thrust bearing three-ball configuration, which significantly reduced the percentage of sliding within the contact region. Hence, it was anticipated that the potential improvement in RCF performance of post-treated thermal spray coatings at higher levels of Hertzian contact stress could be ascertained.

2. Experimental procedure

2.1. Sample preparation

2.1.1. Powder processing and thermal spraying

Two types of agglomerated and sintered powders were prepared for the deposition of the functional graded coating. Specialised nickel alloy powder of composition Ni–7.56% Cr–3.69% Si–2.57% Fe–1.55% B–0.25% C and WC carbides less than 5 μm in size were used to prepare the graded coating. The powder manufacturing route involved pre-alloying the powders, which led to the formation of a spray-dried and sintered composite, which was then sprayed onto the substrates. Pre-alloying has a number of inherent advantages over the other powder manufacturing routes, e.g. mechanical blending. With mechanical blending, WC particles do not melt within the gun and hence on contact with the substrate rebound. In sintered and agglomerated powders, deposit efficiency is significantly higher. Segregation during spraying leads to differences in specific gravity and also the particle size of each powder within the blend, hence it is difficult to achieve a uniform structure. The optimal route of pre-alloying leads to a homogeneous structure. Coatings were deposited on 440-C bearing steel substrates with a JP5000 HVOF system. Prior to the coating process, the substrate material was shot-blasted and preheated to increase the contact area for mechanical interlock and decrease the quenching stresses associated with the impacting lamella. Spraying was carried out using Kerosene as the fuel and oxygen as the powder carrier gas. The gun was kept at a fixed spray distance of 380 mm and the barrel length was measured as 102 mm. The FGM consisted of two layers, which were graded from WC–40% Ni alloy on the substrate to WC–10% Ni alloy on the surface. The average coating thickness of the WC–40% Ni alloy was 100 μm, whilst the thickness of the upper layer of WC–10% Ni alloy after grinding and polishing was 300 μm.

2.1.2. Post-treatment

Coated substrates were Hot Isostatically Pressed (HIPed) at two different temperatures of 850 and 1200 °C in unencapsulated conditions. Samples are normally encapsulated prior to HIPing to prevent surface cracking which can occur

with high temperatures and pressures. However, this safety precaution restricts the complexity in shape for the HIPed components. Since emphasis in thermal spray technology is to continually search for cost effective solutions, an important objective in this analysis was to successfully HIP the coatings without encapsulation. In addition, prior to this investigation, similar coatings were successfully HIPed without encapsulation as the surface of the coating was ground before HIPing to improve resistance to surface cracking. Choice of HIPing temperature was based on the premise that the lower temperature would give minimum distortion to the substrate material, whilst the higher temperature would be beneficial for the microstructural transformation of the coating material. This is consistent with the findings by Nerz et al. [12] where changes in microstructure were reported at about 850 °C. DTA analysis on similar coatings also confirmed an exothermic reaction occurring at 831 and 1100 °C. Changes referring to the heating and cooling rate for both cycles were kept constant at 4 °C/min in order to prevent surface cracking. A constant pressure of 100 MPa on the samples was maintained for 1 h by argon gas being pressurised against the surface of the discs. Under these conditions, none of the coatings exhibited any signs of surface cracking.

In order to investigate the influence of pressure on the microstructure of thermal spray coatings, a number of coated substrates were also vacuum heated at 1200 °C in unencapsulated conditions. The heating and cooling rate was kept constant at 4 °C/min in order to prevent surface cracking.

2.2. Rolling contact fatigue tests

To study the fatigue of highly loaded machine elements such as roller bearings and gears, which are subjected to a combined rolling/sliding motion, extensive tests have to be performed. Since test results of rolling contact fatigue investigations exhibit extensive scatter, many tests are necessary to determine the fatigue life with statistical confidence. It is also difficult to explain the influence of separate parameters on the results because the working conditions of machine elements in industrial practice are not constant. Therefore, test rigs with specimens of simple geometry are favoured to investigate the influence of single parameters on fatigue life. Tourret and Wright [13] have investigated a number of variations on the standard four-ball machine such as type I, II, and III configurations. A number of recent studies have successfully incorporated the type II configuration to test the RCF performance of PVD and thermal spray coated balls and cones [14]. Due to the hostile environment of the heat treatment, it can be difficult to HIP drive balls or cones. Therefore, in the current investigation, steel discs 31 mm in diameter were fabricated, coated and then HIPed. Hence, in changing the shape of the rolling drive element, a number of other modifications to the four-ball machine were necessary in order to maintain the correct rolling/sliding kinematics. These modifications will be discussed in the Section 2.2.1.

A schematic illustration of the modified four-ball machine is shown in Fig. 1. In the current set-up of the assembly, the coated disc was assembled to the drive shaft via a collet and drove three-ball bearings, which act as the rolling elements in the configuration of the deep groove ball bearing. A plastic spacer, which prevents the ball bearings to contact each other during testing, held the ball bearings in position. Three different sizes of spacers were incorporated into the test plan. This enabled more than one test to be performed on each coated disc.

The coated discs were ground and polished to attain a root mean square (RMS) surface roughness of $0.065 \pm 0.015\,\mu m$ (R_q). The ball bearings were commercial grade 440-C bearing steel or hot isostatically pressed silicon nitride ceramic with a surface roughness of $0.01 \pm 0.015\,\mu m$ (R_q). The diameter of the balls was either 4.74, 5.54 or 6.31 mm depending on the diameter of the spacer. RCF tests were conducted under immersed lubrication conditions at a spindle speed of 4000 ± 10 rpm, and at an approximate ambient temperature of 24 °C. Failure was defined as the increase in vibration amplitude above a pre-set level. Two test lubricants; Vitrea 320 and Exxon 2389 were used in the testing program. Vitrea 320 is high viscosity hydrocarbon oil having a kinematic viscosity of $200\,mm^2\,s^{-1}$ at 40 °C. Exxon 2389 is a commercially available synthetic oil having a kinematic viscosity of $12.4\,mm^2\,s^{-1}$ at 40 °C. The ratio (λ) of the elasto-hydrodynamic lubricant (EHL) film thickness to the average surface roughness was calculated using the following relation:

$$\lambda = \left\{ \frac{H_{min}}{(R_{qd}^2 + R_{qp}^2)^{0.5}} \right\} \quad (1)$$

where R_{qd} is the RMS surface roughness of the driving rolling element disc, R_{qp} the RMS surface roughness of the planetary balls, and H_{min} the minimum film thickness and calculated using the following relationship of hard elasto-hydrodynamic lubrication:

$$H_{min} = 3.63U^{0.68}G^{0.49}W^{-0.073}(1 - e^{-0.68k}) \quad (2)$$

where U is the dimensionless speed parameter, G the dimensionless elliptically material parameter, W the dimensionless load parameter and k the dimensionless elliptically parameter. The λ value was approximated as $\lambda > 3$ and $3 > \lambda > 1.5$ for Vitrea 320 and Exxon 2389 lubricants, respectively.

2.2.1. Ball kinematics

The kinematics analysis of the ball bearing set-up can enable a better understanding of the fatigue mechanisms by providing an insight to the surface velocities, micro slip and sliding within the contact region. In lubricated rolling contacts, the phenomena of micro slip within the contact area of contacting bodies, either due to material deformation or due to the differences in the Young's modulus, and lubricant traction can be significantly affected by the kinematics. The objective of the following analysis was thus to calcu-

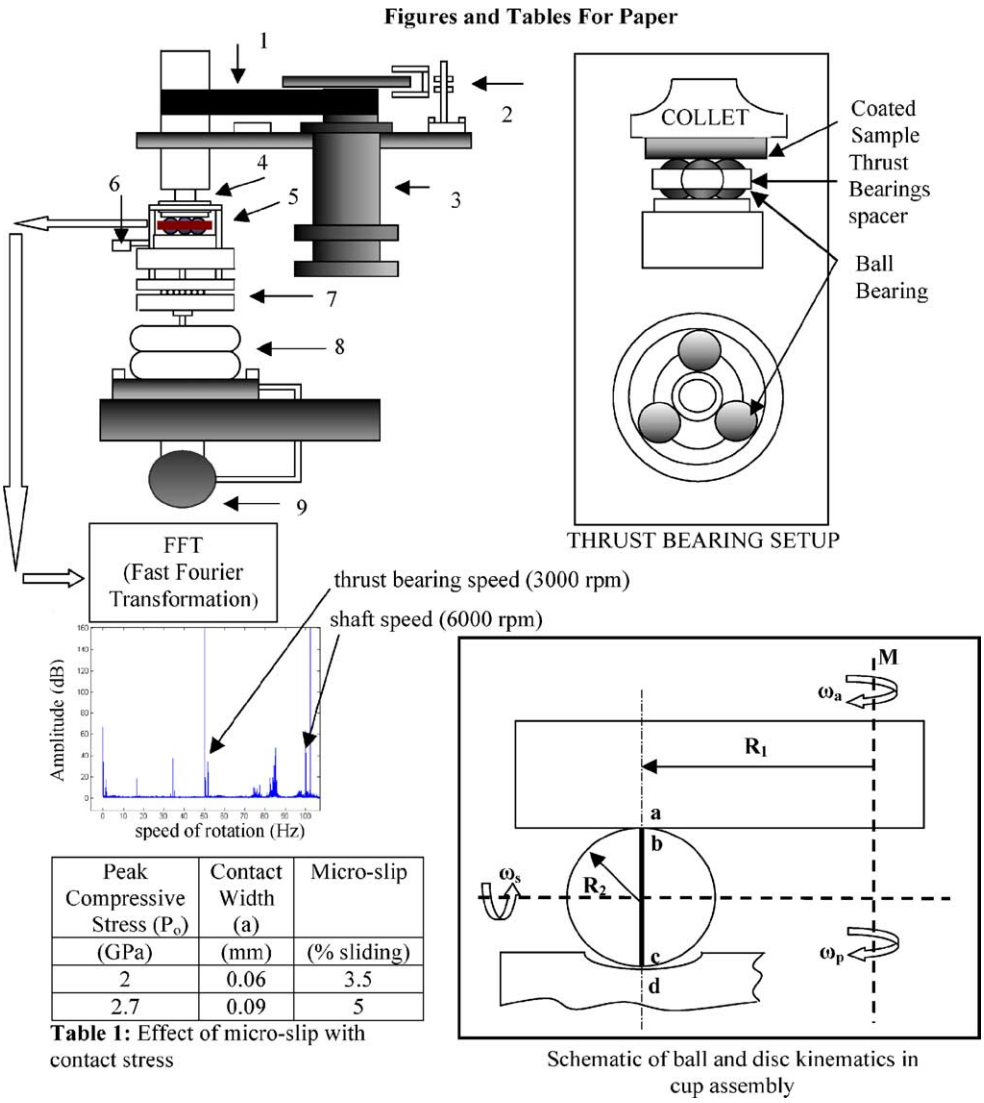

Peak Compressive Stress (P_o) (GPa)	Contact Width (a) (mm)	Micro-slip (% sliding)
2	0.06	3.5
2.7	0.09	5

Table 1: Effect of micro-slip with contact stress

Fig. 1. Schematic illustration of the modified four-ball machine ($R_1 = 7.75$ mm, $R_2 = 6.35$ mm, $\theta = 36.83°$, $\beta = 37.83°$, $\delta = 31.16°$, $\omega = 4000 \pm 10$ rpm). 1, Belt drive; 2, speed sensor; 3, spindle driving motor; 4, coated disc and collet; 5, cup assembly; 6, thermocouple; 7, thrust bearing; 8, bellows; 9, pressure gauge.

late the angular and linear velocities of the coated drive disc and the driven rolling elements for the experimental contact geometry, and then evaluate the micro-slip due to the contact deformation of the materials. This was achieved by considering the instantaneous velocities of the drive plate and the driven rolling elements. Tests were continuously run for a maximum of 70 million stress cycles, since it has been shown in published literature that this is a practical benchmark for evaluating the resistance to rolling contact fatigue [15]. The number of stress cycles per revolution of the drive shaft, known as the stress cycle factor, was thus calculated from the contact kinematics equations.

The kinematics of the modified four-ball machine display an example in which rolling motion is associated with the spin. The three balls held within the plastic spacer orbit about the axis of rotation of the shaft, and at the same time, has a spin component of the velocity inclined to the shaft axis. Consider Fig. 1 in which upper drive disc rotating at a shaft speed contacts the lower ball at point ‘a’. The lower ball contacts the groove in which the ball bearing runs at point ‘c’. The thick line in Fig. 1 shows the wear track formed on the driven ball.

The instantaneous velocity of the drive disc at point ‘a’ (V_a) can be given as

$$V_a = \omega_a R_1 \tag{3}$$

Consider the motion of the planetary balls at point ‘b’. This motion can be divided into two components. About the vertical axis MN and about the axis inclined at 90° to the vertical. The instantaneous velocity of the planetary ball at point ‘b’ (V_b) can be given as

$$V_b = \omega_p R_1 + \omega_s R_2 \tag{4}$$

Assuming no slip at contact of the drive disc and the driven ball:

$$V_a = V_b$$

Equating Eqs. (3) and (4), leads to

$$\omega_a R_1 = \omega_p R_1 + \omega_s R_2 \tag{5}$$

By considering the motion of the planetary ball at point 'c', the instantaneous velocity at point 'c' (V_c) is given as

$$V_c = \omega_p R_1 + \omega_s(-R_2) \tag{6}$$

Assuming no slip between the planetary ball and the thrust bearing holder at points c and d:

$$V_c = V_d$$

$V_d = 0$ (stationary holder).

Hence:

$$\omega_s(-R_2) = -(\omega_p R_1)\omega_s = \frac{\omega_p R_1}{R_2} \tag{7}$$

Substituting Eq. (7) into Eq. (5):

$$\omega_a R_1 = \omega_p R_1 + \left(\frac{\omega_p R_1}{R_2}\right) R_2$$
$$= \omega_p R_1 + (\omega_p R_1) = \omega_p(2R_1),$$
$$\frac{\omega_a}{\omega_p} = \frac{2R_1}{R_1} = 2 \tag{8}$$

The number of stress cycles per revolution of the shaft can be calculated as

$$\text{No. of stress cycles/revolution} = \frac{Z(\omega_a - \omega_p)}{\omega_a} \tag{9}$$

Substituting Eq. (8) and value of Z into Eq. (9):

$$\text{Stress cycle factor} = \frac{3(2\omega_p - \omega_p)}{2\omega_p} = 1.5$$

2.2.2. FFT analysis

Analytical studies to calculate the speed of the lower ball bearings under a given shaft speed and configuration of the modified four-ball system (above) are generally made under the assumption of pure rolling conditions in the four-ball assembly. However, depending upon the tribological conditions such as friction and lubricant behaviour, the actual speeds can be different from the theoretically calculated speeds. Hence, experimental investigation of the orbital speed of the lower ball bearings can not only reveal whether the motion was pure rolling or a combination of pure rolling and sliding, but can also estimate the amount of sliding in the system by comparing the results of experimental investigations with the theoretical calculations.

In order to experimentally investigate the orbital speeds, an accelerometer was connected to the body of the cup assembly. The signal from the accelerometer was relayed to an amplifier. The amplified signal was fed into a computer where dedicated software converted the signal to a digital reading. The data was then processed by Matlab in which using the fast Fourier transformation (FFT) technique, the data was converted to the frequency domain. The technique enabled the precise measurement of the drive shaft speed and average speed of the ball bearings. Fig. 1 shows the results recorded at a shaft speed of 6000 rpm (100 Hz) where the average speed of the ball bearings was 3000 rpm (50 Hz), providing further verification of the kinematics analysis shown in Section 2.2.1.

2.2.3. Slip analysis due to contact conformity

The applied load changes the initial point contact into a well defined contact area, which can be obtained from the Hertz contact analysis. Within this contact region some points may have different tangential velocities from the axis of rotation. This results in micro-slip between the contacting bodies within the contact area, and the effect will be maximum at the edges of the contact area. Williams defined the percentage of slipping as the creep ratio (ξ) which is also called the 'Heathcote' slip:

$$\xi = -\frac{4}{2E^* a}\mu p_0 d^1 \tag{10}$$

where E^* is the contact modulus, a the contact width, p_0 the Hertz contact pressure, μ the coefficient of friction and $d^1 = -a$ at the point of maximum slip [16]. Fig. 1 shows the effect of Hertzian contact stress on the % sliding of maximum slip within the contact region.

3. Experimental test results

Rolling contact fatigue (RCF) tests were conducted under different tribological conditions of Hertzian contact stress and contact configuration. Table 1 displays the conditions for each test, whilst RCF test results are shown in Fig. 2. These results are not intended for statistical fatigue life prediction, but to understand the relative performance of the coated specimens in RCF tests under various conditions of post-treatment. The peak compressive stress values listed in Table 1 were based upon the uncoated case of the contacting rolling elements, giving a conservative comparison, however, it should be noted that the compressive stress in the post-treated coatings was higher (to what is shown in Table 1), due to the increase in coating's elastic modulus after the post-treatment. Maximum tensile stress values listed in Table 1 were based on the experimental measurements of elastic modulus.

3.1. Surface observations

A scanning electron microscope was used to observe the areas of failure on the coated discs. Identification of the

Table 1
Rolling contact fatigue tests for as-sprayed, HIPed at 850 °C, HIPed at 1200 °C and vacuum heated coatings on 440-C bearing steel substrate

Test no.	Contact load, F (N)	Planetary balls	Contact stress, P_0 (GPa)	Contact width (mm)	Depth of maximum shear stress (μm)	Depth of orthogonal shear stress (μm)	Maximum tensile stress (MPa)	Test lubricant	Failure type
As-sprayed tests									
T01	20	Steel	2	0.13	31	23	284	Vitrea 320	Delamination
T02	40	Steel	2.7	0.17	42	30	356	Vitrea 320	Delamination
T03	30	Ceramic	2.7	0.15	35	26	364	Vitrea 320	Delamination
T04	30	Steel	2	0.17	41	30	269	Exxon	Delamination
T05	50	Steel	2.7	0.39	56	41	357	Exxon	Spalling
HIPed at 850 °C tests									
T06	30	Steel	2	0.17	41	30	269	Vitrea 320	Delamination
T07	40	Steel	2.7	0.17	42	30	356	Vitrea 320	Delamination
T08	30	Ceramic	2.7	0.15	35	26	357	Vitrea 320	Delamination
T09	30	Steel	2	0.17	41	30	269	Exxon	Delamination
T10	50	Steel	2.7	0.23	56	41	357	Exxon	Spalling
HIPed at 1200 °C tests									
T11	20	Steel	2	0.15	36	26	256	Vitrea 320	Surface distress
T12	40	Steel	2.7	0.17	42	30	356	Vitrea 320	Surface distress
T13	30	Ceramic	2.7	0.15	35	26	364	Vitrea 320	Surface distress
T14	30	Steel	2	0.17	41	30	269	Exxon	Surface distress
T15	50	Steel	2.7	0.23	56	41	357	Exxon	Surface distress
Vacuum heated tests									
T16	30	Steel	2	0.17	41	30	269	Vitrea 320	Spalling
T17	80	Steel	2.7	0.23	56	41	371	Vitrea 320	Spalling
T18	30	Ceramic	2.7	0.14	35	26	364	Vitrea 320	Delamination
T19	30	Steel	2	0.17	41	30	269	Exxon	Delamination/surface distress
T20	50	Steel	2.7	0.23	56	41	357	Exxon	Surface distress

failure modes required the width of the wear track to be calculated since one of the main methods for characterising the type of failure was by determining if the failure had spread out with the width of the wear track. The theoretical width of the wear track was calculated using the Hertzian circular point contact equation:

$$2a = 2\left(\frac{3FR}{4E^*}\right)^{1/3} \tag{11}$$

The calculated width of wear track for each test is listed in Table 1. To check the theoretical calculations, the wear track of a failed coated discs which displayed no evidence

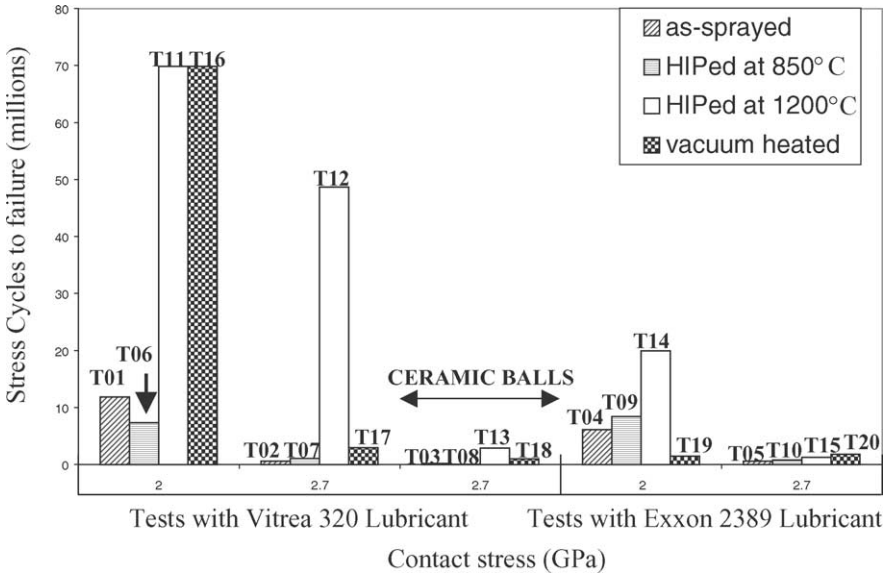

Fig. 2. Rolling Contact Fatigue Results for as-sprayed, HIPed at 850 °C, HIPed at 1200 °C and vacuum heated coatings.

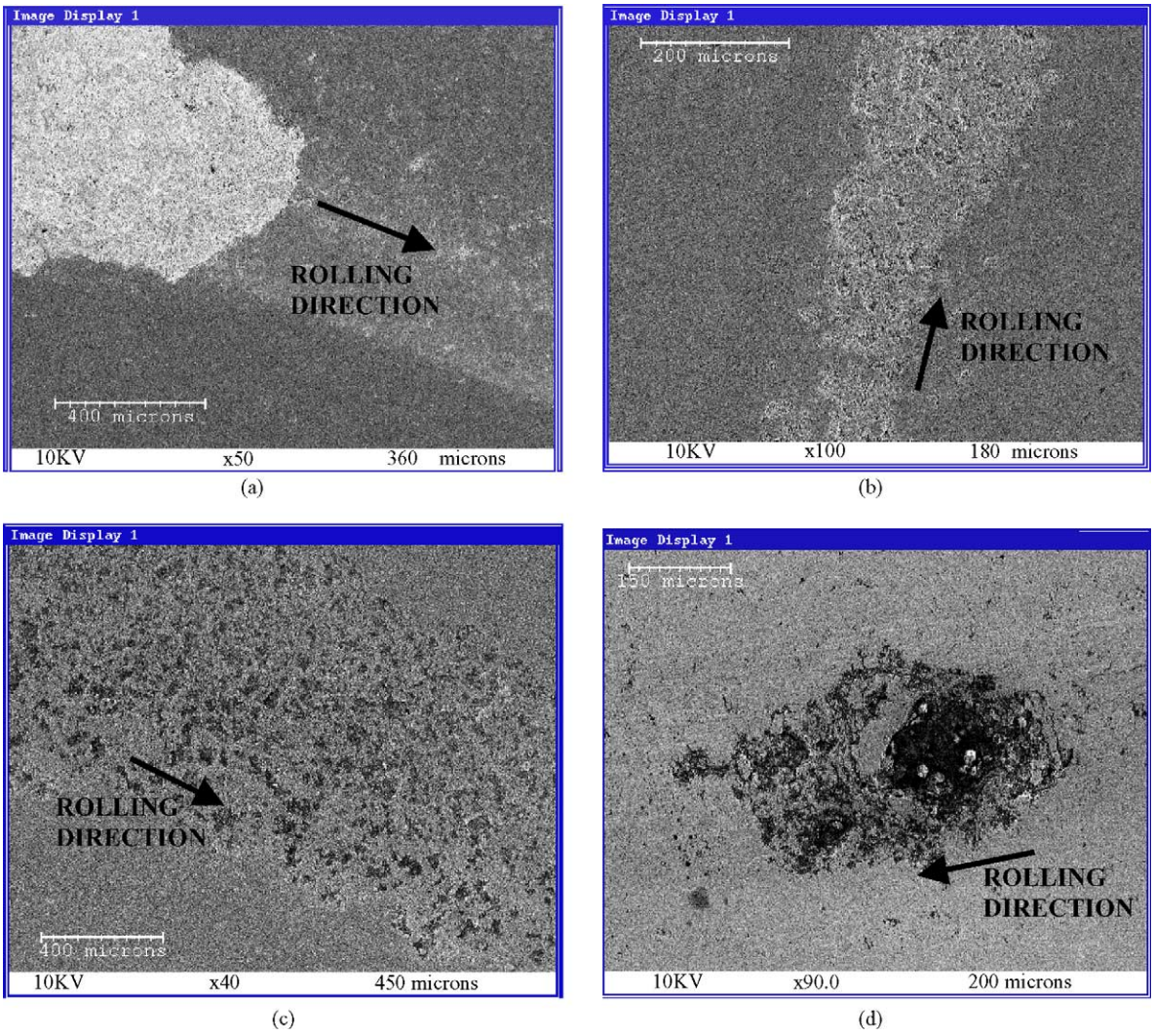

Fig. 3. Surface observations for WC–NiCr coatings tested at 2 GPa contact stress using steel balls (test T01, T06, T11, T16): (a) as-sprayed coating (test T01); (b) HIPed at 850 °C coating (test T06); (c) HIPed at 1200 °C coating (test T11); (d) vacuum heated coating (test T16).

of surface distress (surface distress can spread out with the wear track) were measured, which compared well with the theoretical values.

Fig. 3 displays the surface observation of failed coatings tested at a contact stress of 2 GPa. Fig. 3(a) shows the surface observation of the as-sprayed WC–NiCr failed coated disc (T01). Surface failure was in the form of delamination since the area of failure was wider than the width of the wear track. Fig. 3(b) shows the surface observation of a HIPed at 850 °C failed coated disc, which was tested under identical tribological conditions. Coating has delaminated from the wear track. At higher HIPing temperature of 1200 °C, a high frequency of micro-pits were observed within the wear track of the failed coated disc (T11) as shown in Fig. 3(c). Fig. 3(d) displays the surface observation of a failed vacuum heated coated disc. Mode of failure was identified as spalling within the wear track.

Fig. 4 shows the surface observations of the failed coated discs tested under identical tribological conditions and at a higher Hertzian contact stress of 2.7 GPa. Fig. 4(a) displays the surface observation of an as-sprayed failed coated disc. Spalling was identified on the wear track. Fig. 4(b) displays the surface observation of a failed post-treated coated disc (T07). HIPing at 850 °C led to the formation of identifiable cracks at the edge of the delaminated area. Fig. 4(c) shows the surface observation of a failed coated disc HIPed at 1200 °C (T12). A high frequency of micro-pits are observed within the wear track. In contrast the failed vacuum heated coating displayed spalling as the main failure mode, as shown in Fig. 4(d).

Fig. 5 displays the surface observations of the as-sprayed and post-treated coatings subjected to a contact stress of 2.7 GPa using ceramic balls. Fig. 5(a) shows the surface observation of an as-sprayed failed coated disc (T03). It can be seen that the coating has delaminated from the wear track. Observation of the HIPed at 850 °C coated disc (T08) in Fig. 5(b) also displays evidence of coating delamination. Delamination differs from spalling failure in that the failure

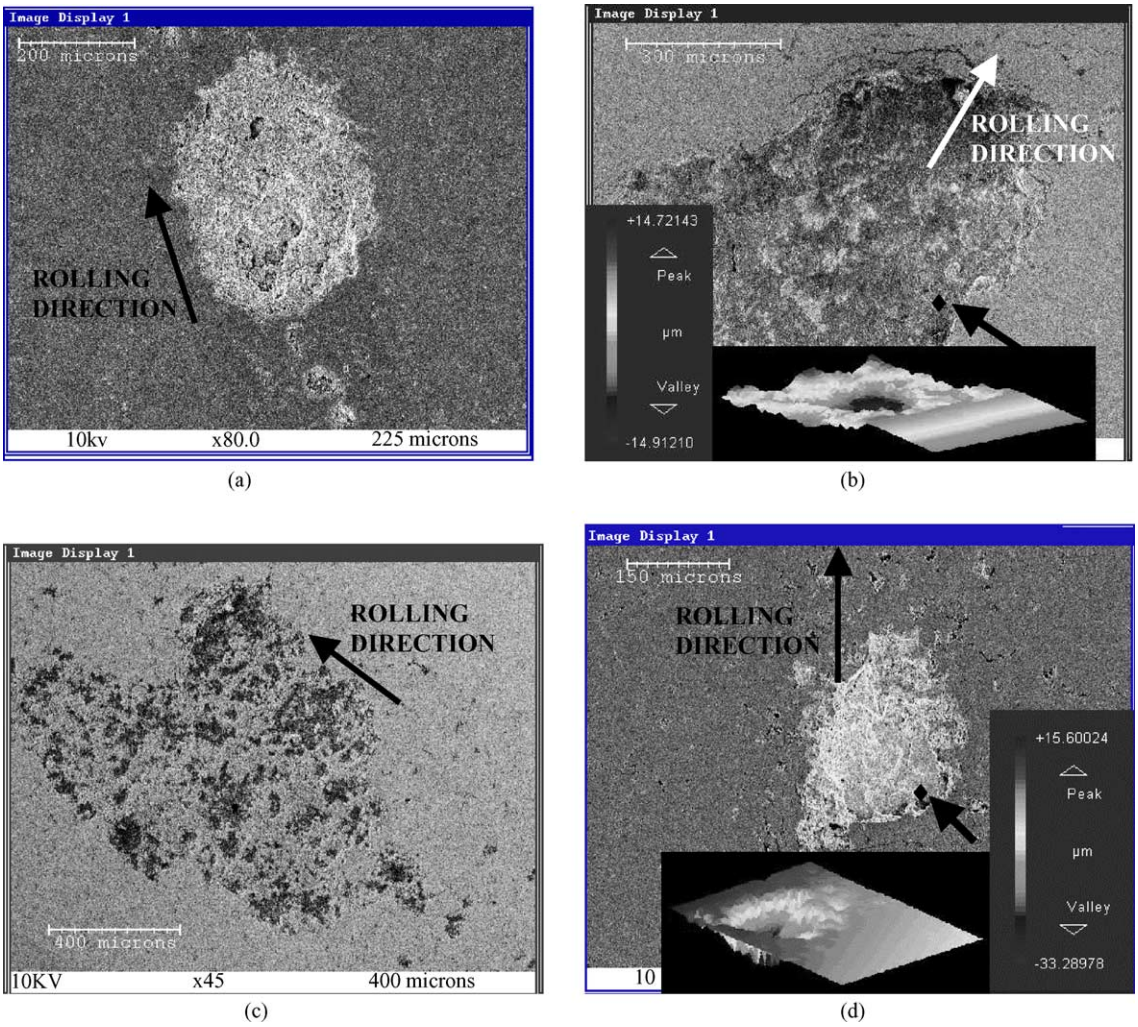

Fig. 4. Surface observations for WC–NiCr coatings tested at 2.7 GPa contact stress using steel balls (test T02, T07, T12, T17): (a) as-sprayed coating (test T02); (b) HIPed at 850 °C coating (test T07); (c) HIPed at 1200 °C coating (test T12); (d) vacuum heated coating (test T17). The arrow marking the ◆ indicates the location of 3D interferometric plot.

is normally deeper, bigger in area and hence, spreads out of the wear track. Surface observation of the failed coated disc HIPed at 1200 °C (T13) in Fig. 5(c) shows a number of micro-pits within the wear track as well as evidence of micro-cracking. Fig. 5(d) shows the surface observation of a failed vacuum heated coated disc (T18). Mode of failure was characterised as delamination since a large pit was observed which had spread out with the confines of the wear track.

Fig. 6 shows the surface observations for coatings subjected to a contact stress of 2 GPa using steel balls but a lubricant of lower viscosity, thus shifting the film regime at contact from full film to mixed film regime. Fig. 6(a) shows the surface observation of a failed as-sprayed coated disc (T04). A number of micro-cracks have initiated from the edge of the wear track and propagated inwards towards the centre of the wear track. The intersection of micro-cracks at the centre of the wear track resulted in coating delamination. Fig. 6(b) shows the surface observation for a failed coated disc HIPed at 850 °C (T09). Significant coating delamination is identified as well as macro-cracks at the edge of the wear track.Fig. 6(c) shows the surface observation for a failed coated disc HIPed at 1200 °C (T14). Macro-cracking is observed at the edge of the contact region. In Fig. 6(d) initial observation indicates no evidence of failure, however, closer inspection shows the width of the wear track is significantly wider than the expected width (Table 1). The depth of failure listed in Table 2 indicated failure as surface distress and delamination (T19).

Fig. 7 shows the surface observations for as-sprayed and post-treated coatings subjected to a contact stress of 2.7 GPa using steel balls and Exxon lubricant. Fig. 7(a) shows the wear track of the failed as-sprayed coated disc (T05). Spalling is observed on the wear track and micro-cracks are visible at the edge of the spall. Spalling is also identified as the mode of failure for the failed coating HIPed at 850 °C (Fig. 7(b)). The spall is located in the centre of the wear track however, a crack connects the spall to the edge of the contact region. Observation of the failed coating HIPed

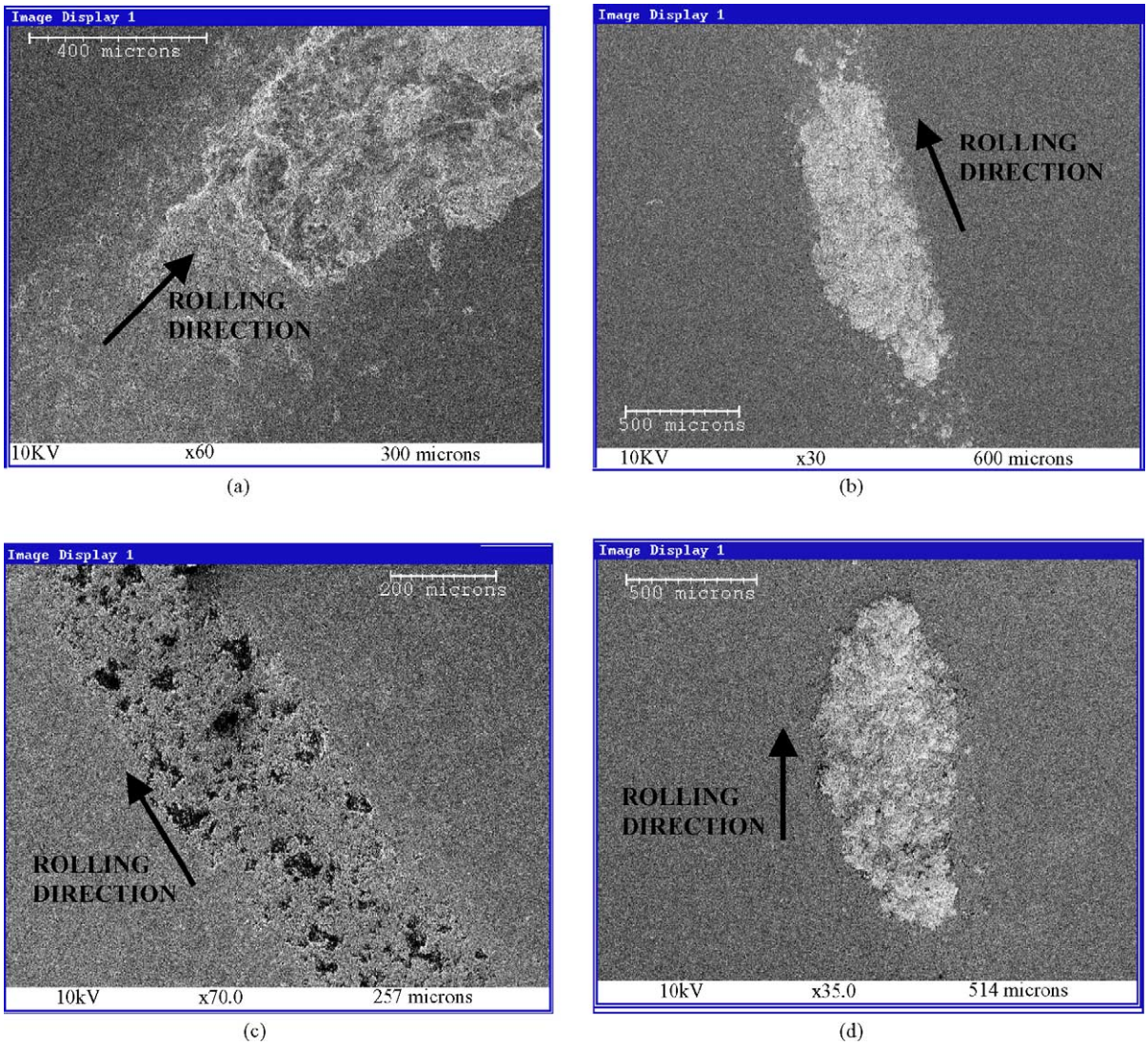

Fig. 5. Surface observations for WC–NiCr coatings tested at 2.7 GPa contact stress using ceramic balls (test T03, T08, T13, T18): (a) as-sprayed coating (test T03); (b) HIPed at 850 °C coating (test T08); (c) HIPed at 1200 °C coating (test T13); (d) vacuum heated coating (test T18).

at 1200 °C showed sheet like debris has delaminated from the wear track. Fig. 7(d) shows the wear track of the failed vacuum heated coating. Propagation of micro-cracks initiating at the edge of the contact region has led to coating delaminating from the centre of the wear track.

3.2. Microstructural observations

The microstructure of the as-sprayed and post-treated coatings was observed under back scattered SEM. Fig. 8 shows the observations of the as-sprayed WC–NiCr functional graded coating. Fig. 8(a) shows the overall view of the coating microstructure. Fig. 8(b) shows a detailed image of the upper layer. The lower layer is displayed in detail in Fig. 8(c). The difference between Fig. 8(b) and (c) was attributed to the higher percentage of binder in the lower layer. In both layers carbides can be clearly identified and are quite spherical in shape. Fig. 8(d) shows the interface between the lower layer and substrate. A definite interfacial line is observed between the two layers.

Fig. 9 shows the cross-section observations of the coating HIPed at 850 °C. Fig. 9(a) shows the microstructure of the coating. The two separate layers of the FGM are clearly visible. Fig. 9(b) shows the microstructure of the upper layer at high magnification. The carbides can be clearly identified and are spherical in shape. The lower layer is shown in detail in Fig. 9(c). Fig. 9(d) shows the interface between the lower layer and substrate.

Fig. 10 shows the observations of a coating HIPed at the elevated temperature of 1200 °C. Fig. 10(a) shows the coating/substrate interface. A separate diffusion layer has formed between the lower layer of the coating and the substrate. This diffusion layer was not observed in either the as-sprayed or HIPed at 850 °C coatings. Fig. 10(b) shows the microstructure of the upper layer in detail. The carbides have reduced in size and compacted together. Fig. 10(c) shows the mi-

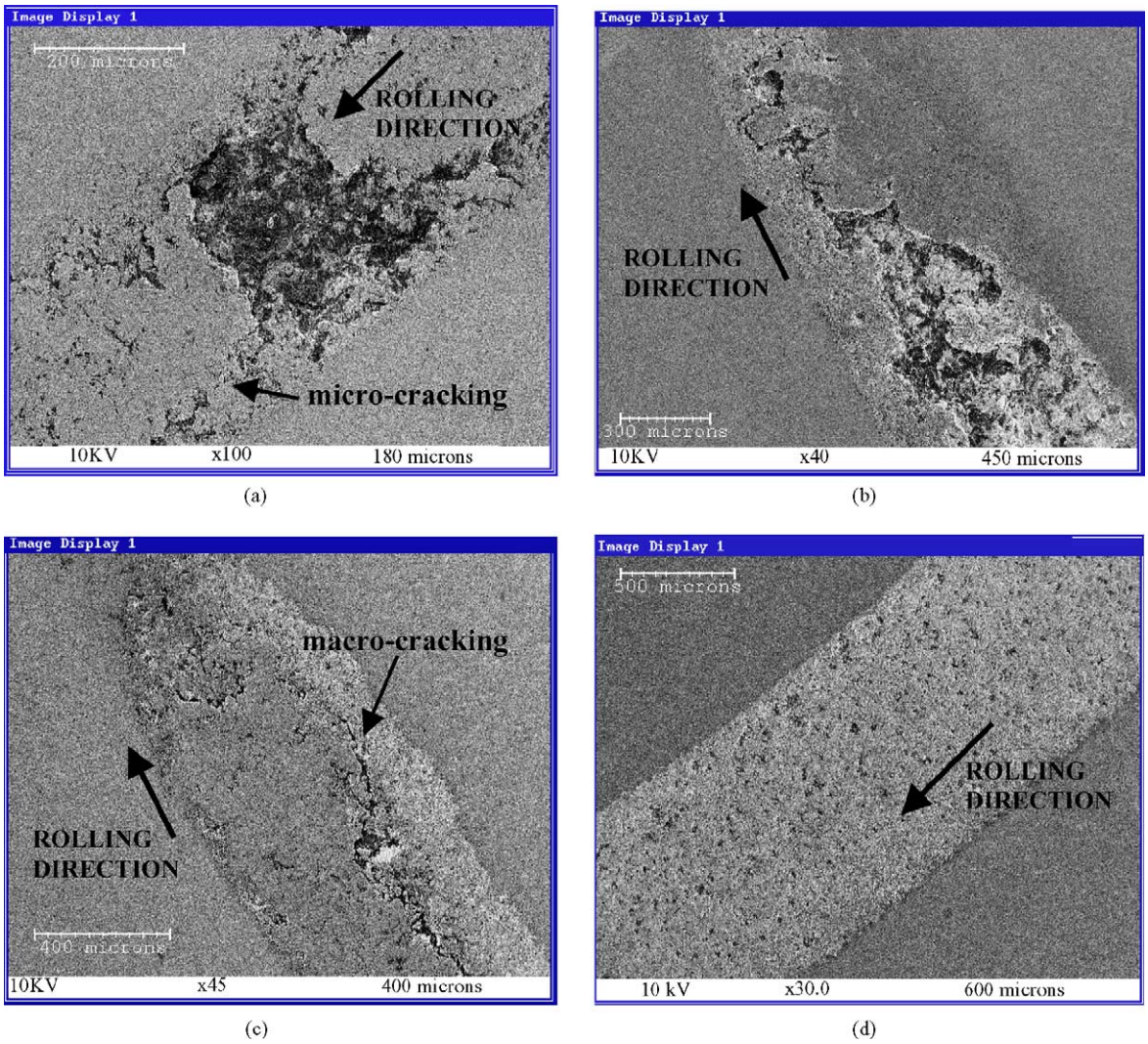

Fig. 6. Surface observations for WC–NiCr coatings tested at 2 GPa contact stress using Exxon lubricant (test T04, T09, T14, T19): (a) as-sprayed coating (test T04); (b) HIPed at 850 °C coating (test T09); (c) HIPed at 1200 °C coating (test T14); (d) vacuum heated coating (test T19).

crostructure of the lower layer at high magnification. The carbides have not only changed shape but are also contacting. The interface between the two layers at high magnification is shown in Fig. 10(d). The lower layer is identified by the higher percentage of binder visible.

Fig. 11 shows the observations of a coating vacuum heated at 1200 °C. Fig. 11(a) shows the interface of the coating and substrate. A diffusion layer can be observed between the coating and substrate and also a degree of porosity close to the interface. Fig. 11(b) shows the microstructure of the lower layer in greater detail.

3.3. Micro-hardness and indentation modulus analysis

Hardness and indentation modulus measurements were performed on the as-sprayed and post-treated thermal spray coatings. Indentation modulus values were obtained using a nano indentation system.

Micro-hardness and indentation modulus measurements were taken on the surface and cross-section of as-sprayed, HIPed at 850 °C, HIPed at 1200 °C and vacuum heated discs. Hardness measurements were taken on the surface and on the cross–section of the coatings at an indentation load of 2.9 N. Results are displayed in Fig. 12(a). Results from the as-sprayed coating show a surface hardness of 845 HV. In comparison, results from the surface of the coating HIPed at 850 °C display a slight increase in hardness of 965 HV. Increasing the HIPing temperature to 1200 °C led to an increased surface coating hardness of 1189 HV. The vacuum treated coating had an average surface hardness of 1206 HV.

Hardness measurements taken on the cross-section indicated similar trends as observed in the surface hardness values, however indentations made on the lower layer of the FGM yielded some unusual results. As-sprayed coatings showed a hardness of 1060 HV at 350 μm. Coating HIPed at 850 °C exhibited a lower hardness of 862 HV at this depth.

Table 2
Depth analysis of as-sprayed, HIPed at 850 °C, HIPed at 1200 °C and vacuum heated discs

Test no.	Depth of failure (μm)	Orthogonal shear stress depth (μm)	Maximum shear stress depth (μm)
T01	35	23	31
T02	38	30	42
T03	46	26	35
T04	32	23	31
T05	40	41	56
T06	18	23	31
T07	23	30	42
T08	20	26	35
T09	46	30	41
T10	43	41	56
T11	28	26	36
T12	22	30	42
T13	17	26	35
T14	8	30	41
T15	33	41	56
T16	31	30	41
T17	38	41	56
T18	15	26	35
T19	33	30	41
T20	12	41	56

HIPed at 1200 °C and vacuum treated coatings displayed similar hardness values at this depth of 783 and 729 HV, respectively.

Indentation modulus results are shown in Fig. 12(b). Measurements were taken on both the surface and cross-section at a test load of 500 mN. Results from the surface of the as-sprayed coating displayed an average value of 250 GPa. Results from the surface of the coating HIPed at 850 °C displayed a slightly higher value of 300 GPa. On increasing the HIPing temperature to 1200 °C, a slight increase in the indentation modulus was observed from the surface measurements. However, surface value for vacuum heated coating was 500 GPa which was significantly higher than all other coatings. Indentation modulus results on the cross-section of the coating within the upper layer of the FGM were observed to be higher in the HIPed coatings. Indentation modulus results for the as-sprayed coating remained constant at 185 GPa through out the upper layer. Results for the vacuum heated coating dropped in moving away from the surface and at a depth of 250 μm also displayed an average value of 185 GPa. In comparison, HIPed coatings displayed significantly higher values at this depth.

3.4. Depth analysis of coating failures

Depth analysis of the areas of failure on the wear tracks of the tested coatings enabled further insight into the origin of failure initiation. These measurements were taken using a scanning white light interferometer. Results can indicate areas of weakness within the FGM which arose from residual stresses due to differences in thermal expansion coefficients, and also due to coating defects. Previous investigations have attributed sub-surface failure to the location of either maximum shear or orthogonal shear stress. Hence, in Table 2, depths of failure and location of maximum shear and orthogonal shear stress are listed for the tests. Typical examples of the 3D interferometric images of the failures used to ascertain the depth values in Table 2 can be seen in Fig. 4(b) and (d).

3.5. X-ray diffraction

The phase composition of the as-sprayed and post-treated coatings was characterised using a D500 X-ray diffractometer, operating at 40 kV and 20 mA with Cu Kα radiation (1.5406 Å, step size of 0.02° and dwell time of 2 s). The samples were run at 2θ from 20° to 100° to investigate the phase transformations that occurred during the coating deposition and post-treatment. XRD spectrums for the WC–10% NiCr layer in both as-sprayed and post-treated coatings are presented in Fig. 13.

4. Discussion

4.1. Influence of coating microstructure

4.1.1. As-sprayed coatings

Fig. 12 shows the XRD spectrum of the upper layer of the as-sprayed coating. A broad amorphous hump was observed between 42° and 44° and two separate peaks identified as W_2C phases. The following reaction occurred during spraying:

$$2WC \rightarrow W_2C + C \quad (12)$$

$$W_2C \rightarrow 2W + C \quad (13)$$

Reactions (12) and (13) occur due to the decarburisation process which is kinetically driven and has been well documented in previous investigations on thermal spraying [17]. The degree of decarburisation is related to the manufacturing process of the powder, the deposition process flame temperature and velocity. The lower flame temperature experienced in the HVOF process results in less reactions in the carbide particles during spraying, though some decomposition occurs as the use of agglomerated and sintered powders, which may lead to a higher degree of carbide dissolution. Fig. 7 shows the microstructure of the as-sprayed coating. In both the upper and lower layers of the FGM, two distinct matrix and carbide types were observed. The matrix marked (A) is very dark indicating a low mean atomic number. The carbide grains within it were of an angular and blocky morphology (B). The second type of matrix observed (C) was much brighter (indicating a higher mean atomic number) and the carbides which it encapsulated were smaller, rounder and had a brighter rim. The rim of second phase material was identified as W_2C. In this region the carbides have dissoluted in the liquid NiCr during spraying forming Ni_2W_4C (amorphous hump). The surrounding matrix was enriched in both carbon and tungsten (leading to its brighter contrast

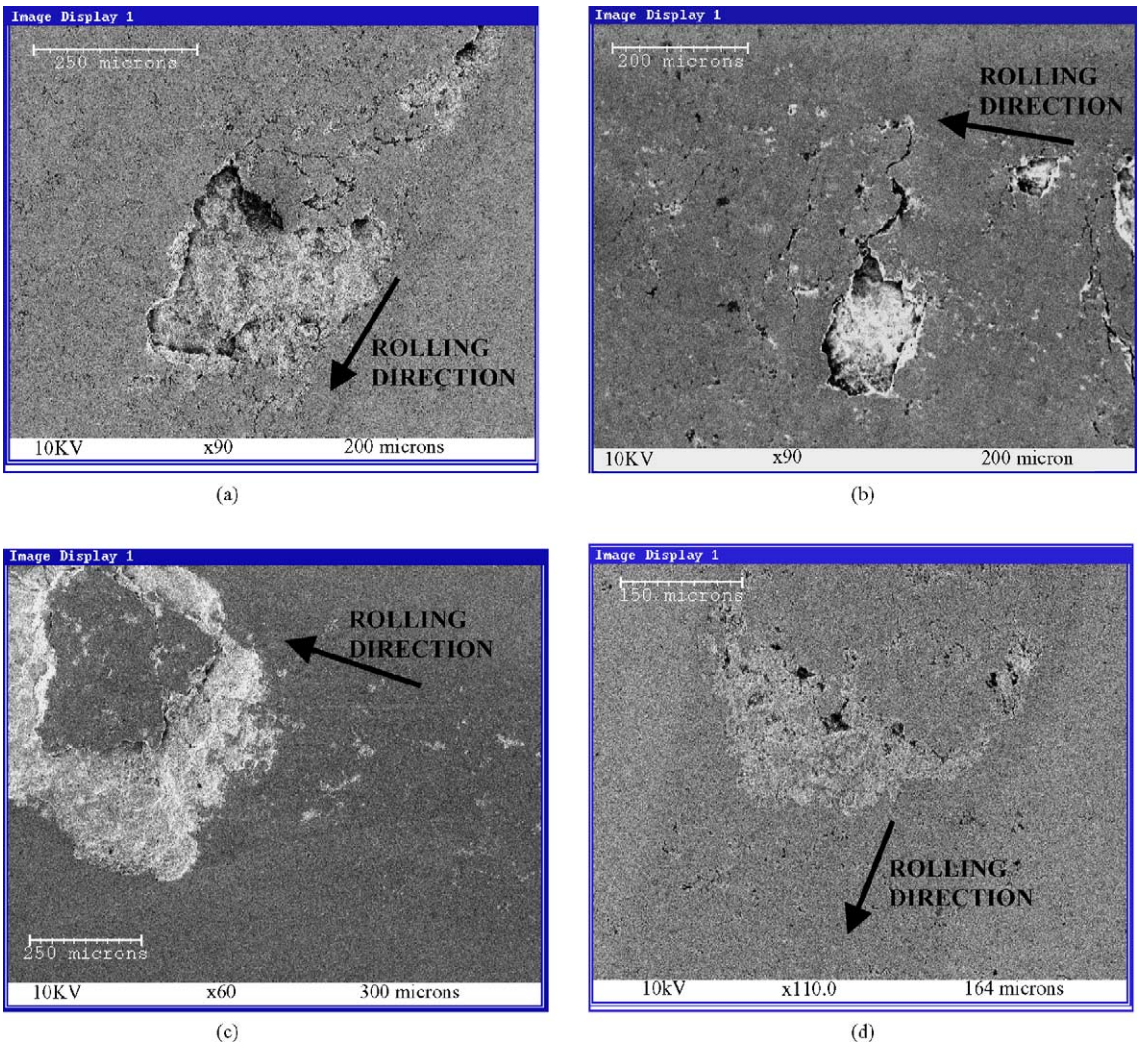

Fig. 7. Surface observations for WC–NiCr coatings tested at 2.7 GPa contact stress using Exxon Lubricant (test T05, T10, T15, T20): (a) as-sprayed coating (test T05); (b) HIPed at 850 °C coating (test T10); (c) HIPed at 1200 °C coating (test T15); (d) vacuum heated coating (test T20).

in the back scattered electron image) and leaving a rim of W_2C surrounding the WC particle. The regions in the coating which showed greater reactions between the binder and the carbide were at the outer regions of the original carbides where higher temperatures were experienced during spraying. It is interesting to note that in previous investigations [9], cracking has been seen in the region of the binder enriched with tungsten and carbon, although not seen in this investigation due to the magnification limit of back scattered electron imaging. This indicates that this phase was brittle which could lead to relatively poor RCF performance.

The change in microstructure between the upper and lower layer of the FGM resulted in slightly different mechanical properties as shown in Fig. 12. The micro-hardness of the lower layer was slightly higher than the values obtained for the upper layer. Although not reported in this investigation a number of crystalline phases were observed in the XRD pattern of the lower layer ($Cr_{23}C_6$, Ni_2C_x), which were not observed in the upper layer XRD spectrum as shown in Fig. 13. The combination of these crystalline phases and an increased percentage of matrix (40% NiCr) within the lower layer, led to increased binder strength as a result of alloying during spraying.

4.1.2. HIPed at 850 °C coatings

The microstructure of the upper layer of the HIPed at 850 °C coating was similar to the microstructure of the as-sprayed coating however, the XRD pattern indicated a reduction in the intensity of the amorphous phase as well as the formation of a new peak identified as $Cr_{23}C_6$. DTA analysis of WC coatings indicates that an exothermic reaction occurs at about 831 °C [18]. At this temperature, the amorphous phase starts to crystallise to form complex carbides with the precipitation of free carbon. The lack of tungsten in the XRD spectrum suggests the tungsten and carbon were consumed by Ni solid solution to form the intermetallic complex carbide Ni_2W_4C, which was too low in intensity to be observed in the XRD spectrum at this post-treatment

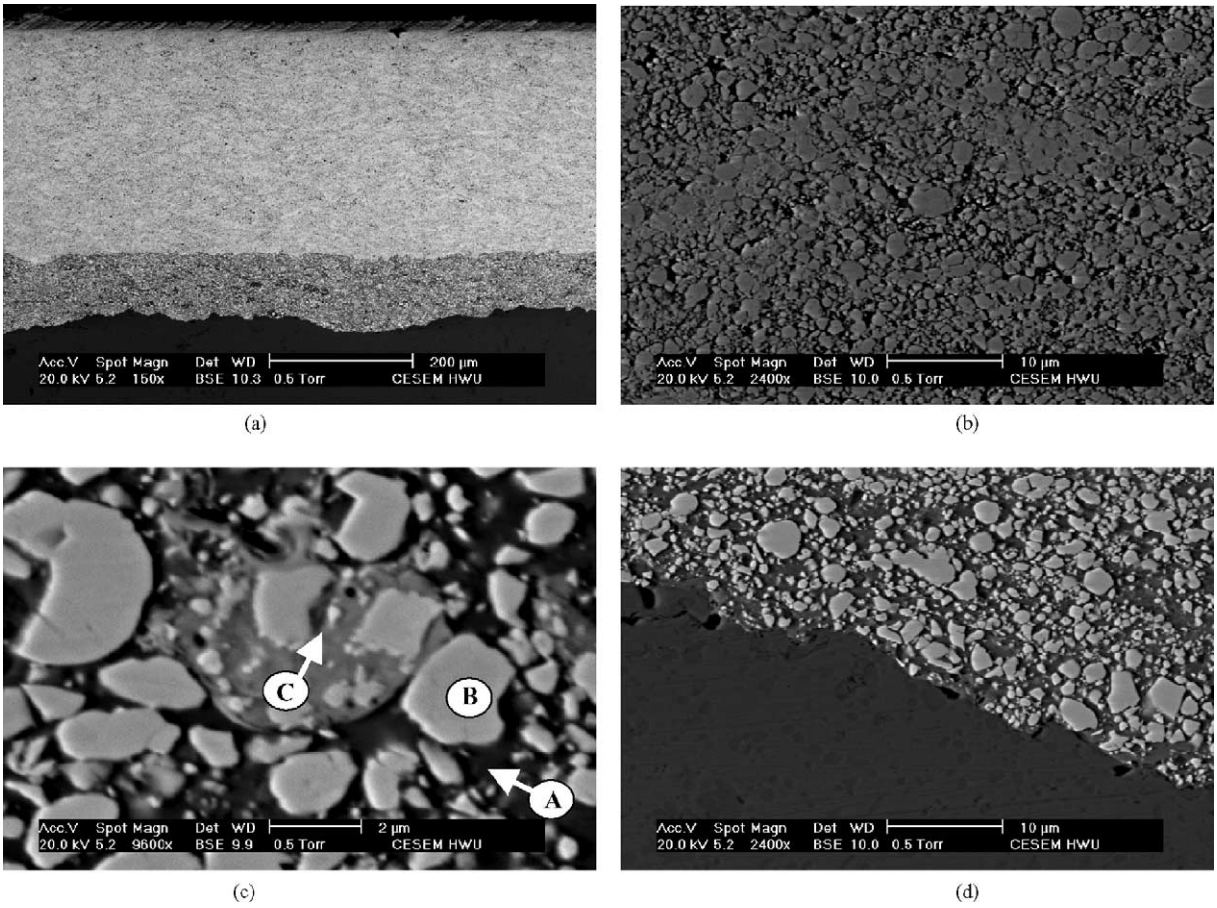

Fig. 8. Microstructural observations for as-sprayed WC–NiCr coating: (a) coating; (b) upper layer of FGM; (c) lower layer; (d) upper/lower layer interface.

temperature. Since the amorphous hump was still observed, it is likely this will have an adverse effect on the RCF performance.

The mechanical properties of the coating changed with HIPing at 850 °C. Dissolution of carbides resulted in solid state sintering and the formation of physical bonds between the mechanically interlocked splats, hence the values for elastic modulus increased with HIPing, and in particular, the average value for the upper layer was higher than the lower layer. Due to the complexity of the coating microstructure, a number of hardness mechanisms were responsible for the changes in hardness with HIPing at 850 °C. For WC cermets, the model of Lee and Gurland [19,20] has been commonly applied.

$$H_C = H_{WC}V_{WC}C + H_M(1 - V_{WC}C) \quad (14)$$

The cermet hardness (H_C) is based on the hardness and volume fraction of the hard phase (H_{WC} and V_{WC}) and the hardness of the matrix phase (H_M). The contiguity (C) defined by Gurland describes the percentage surface area of a carbide grain in contact with other carbide grains and accounts for the microstructural influence of the carbide morphology. The hardness of the two phases is microstructure dependent. Carbide hardness is a function of grain size, smaller grains giving higher hardness values. With regard to the overall cermet hardness, a higher degree of contiguity generates harder material. In addition, for thermally sprayed cermet coatings, splat to splat bonding will also affect the overall hardness. In the lower layer, recovery, recyrstallisation and grain growth occur rapidly, reducing the dislocation density, increasing the grain size and relieving any internal stresses within the splats. These transformations lead to carbide dissolution and account for the reduction in hardness in the lower layer as observed in Fig. 12. Within the upper layer, the reduction in binder led to a higher percentage of dissolved tungsten and free carbon within the binder which inhibited dislocation motion [21]. The structural disorder caused by the higher percentage of dissolved W and C was observed in the broader XRD peaks for the matrix phase in the upper layer. The extent of binder phase was dependent on the deposition parameters being more influential in the higher temperature techniques where extensive carbide dissolution meant that the layer acted more as a dispersion strengthened alloy than a carbide based composite.

4.1.3. HIPed at 1200 °C coatings

The microstructure of the coating changed significantly after HIPing at the elevated temperature of 1200 °C as shown in Fig. 10. In the upper layer, significant contact had occurred between the carbides and a number of micro-voids

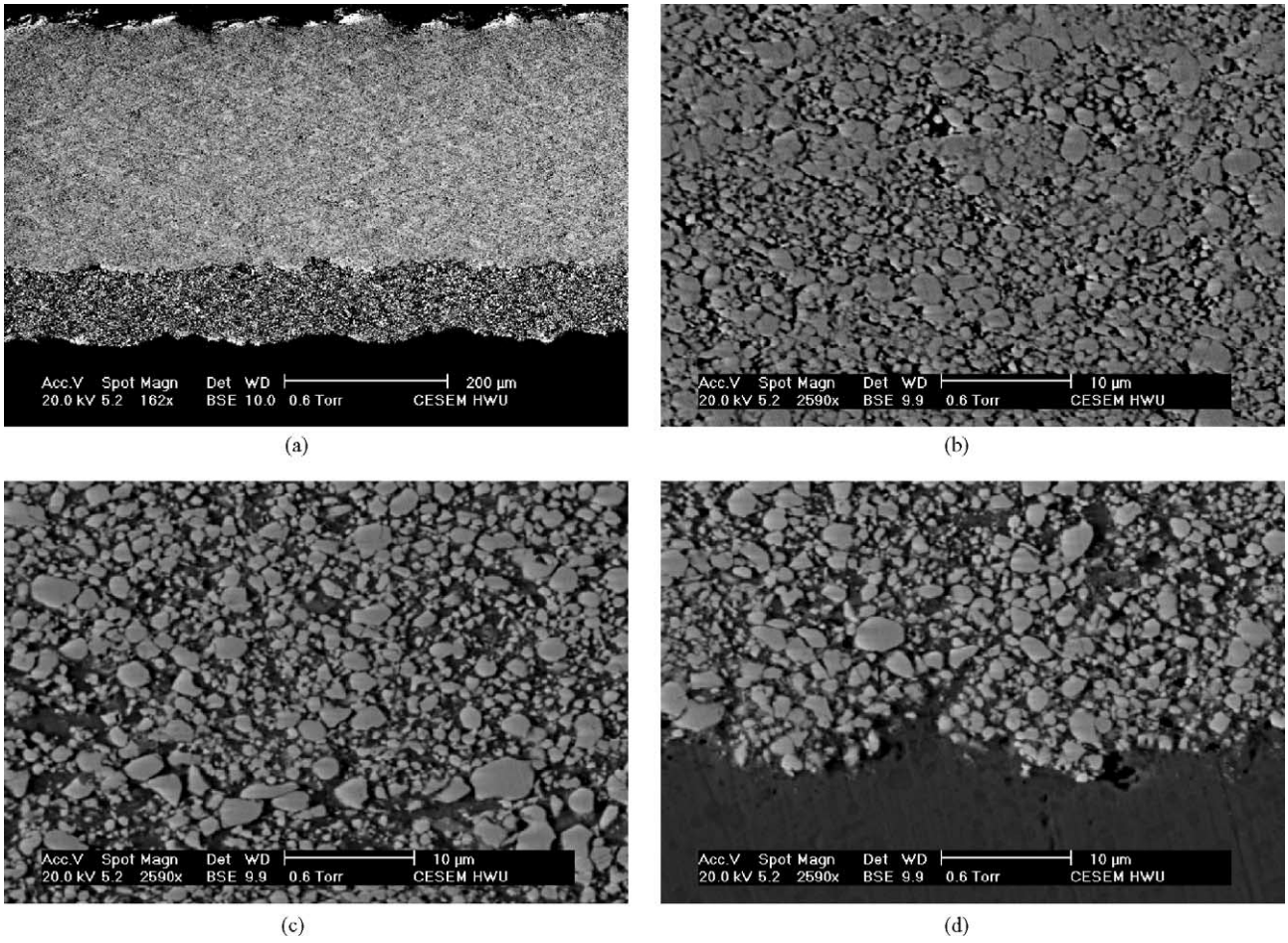

Fig. 9. Microstructural observations for HIPed at 850 °C WC–NiCr coating: (a) coating; (b) upper layer of FGM; (c) lower layer; (d) upper/lower layer interface.

were observed in the centre of the carbides. Similar characteristics were observed in the lower layer, however in addition, the carbides were slightly darker at the boundaries with the binder and an inter-diffusion layer was observed at the coating/substrate interface. The XRD pattern showed that the amorphous hump had disappeared and a number of new narrow peaks were visible. The new peaks were identified as complex carbides (Ni_2W_4C, Fe_3W_3C). The W_2C peak was also no longer visible.

At elevated temperatures, the reaction ($4WC + 2Ni \rightarrow Ni_2W_4C + 3C$) and reaction ($3WC + Fe \rightarrow FeW_3C + 2C$) takes place during the recrystallization of the amorphous phase and form eta-carbides. The enriched tungsten and carbon which existed within the amorphous phase was consumed by Ni and Fe. Dissolution of the WC carbides and formation of FeW_3C also resulted in the free carbon to assist the formation of complex chromium carbides such as $Cr_{23}C_6$ seen in the XRD spectrum. Fig. 10(c) shows the two different carbides within the matrix. The darker carbide has formed from recrystallization of the amorphous region. EDX analysis of this region showed a high percentage of nickel and tungsten but a relatively low percentage of chromium within this region, which suggests evidence of a nickel based carbide. Chromium carbides were forming elsewhere in the microstructure from carbide dissolution. The diffusion layer observed at the coating/substrate interface has been observed in previous investigations on the post-treatment of WC–NiCr coatings, and EPMA analysis showed that this interfacial layer contained predominantly nickel, though chromium and iron were also observed.

The formation of a diffusion layer was the result of the Kirkendall effect and is the end result of two chemical species (Ni and Fe) diffusing in opposite directions at different rates [10]. Proof of the Kirkendall effect is verified by Kirkendall pores in either the coating next to the diffusion layer or at substrate, however, unlikely to be seen in the coatings as they were reduced in size due to compaction during HIPing. Nickel is the dominant species in the diffusion layer because nickel diffuses from the coating across the diffusion layer into the substrate more rapidly than Iron in the opposite direction, leading to unequal fluxes of the two species from different directions (Kirkendall effect). A net diffusional mass flows from the coating to the substrate representing the diffusion layer growing by consuming the coating. As the diffusion layer moves towards the substrate, an excess of vacancies which later become pores (Kirkendall

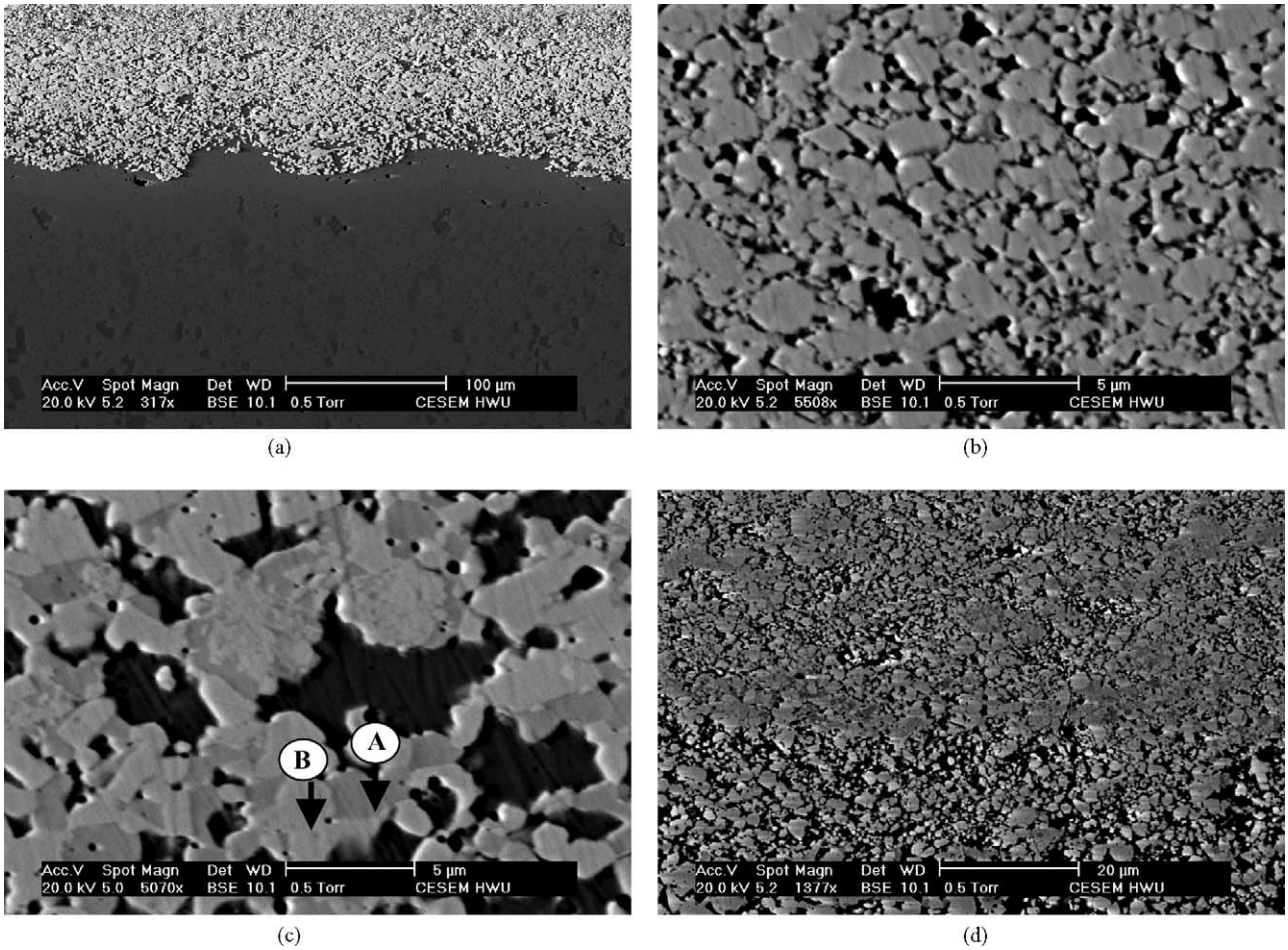

Fig. 10. Microstructural observations for HIPed at 1200 °C WC–NiCr coating: (a) coating; (b) upper layer of FGM; (c) lower layer; (d) upper/lower layer interface.

pores) form in the coating neighbouring the diffusion layer. As the diffusion layer moves towards the coating, the Kirkendall pores become part of the diffusion layer. When the coating is subjected to HIP treatment, the Kirkendall pores can be partially closed up or reduced in size due to compaction which increases the contact area between the coating and the diffusion layer and thus speeds up element diffusion and transition layer growth.

The mechanical properties were significantly influenced by the changes within the coating microstructure. The hard-

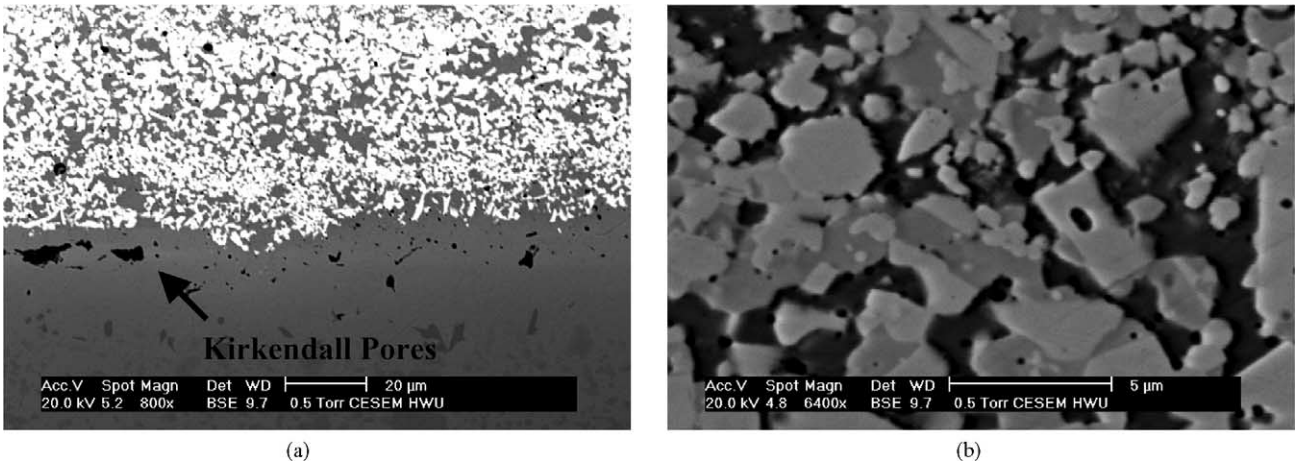

Fig. 11. Microstructural observations for vacuum heated WC–NiCr coating: (a) coating; (b) upper layer of FGM.

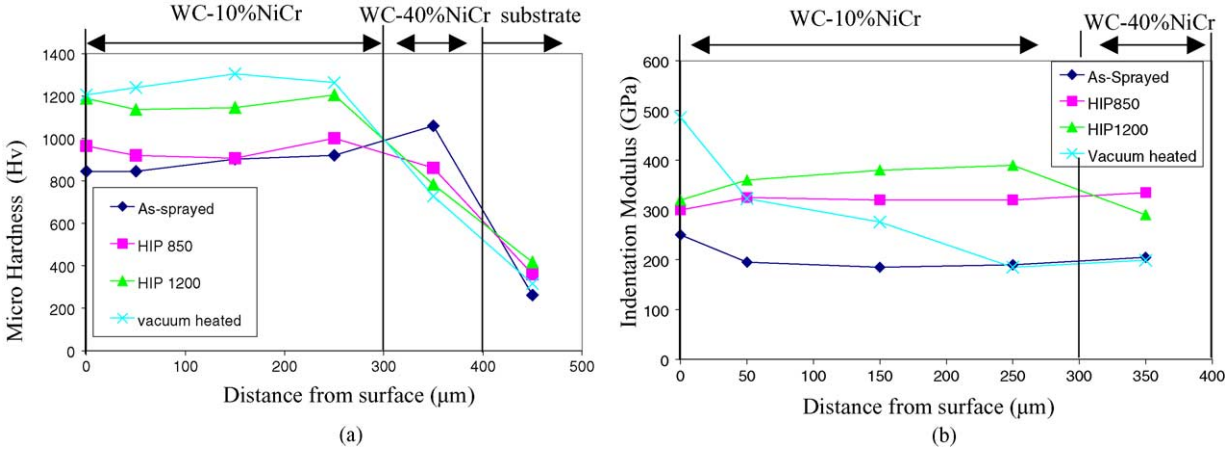

Fig. 12. Microstructural analysis of coatings: (a) micro-hardness results for as-sprayed, HIPed at 850 °C, HIPed at 1200 °C, vacuum heated coatings; (b) indentation modulus results for as-sprayed, HIPed at 850 °C, HIPed at 1200 °C, vacuum heated coatings.

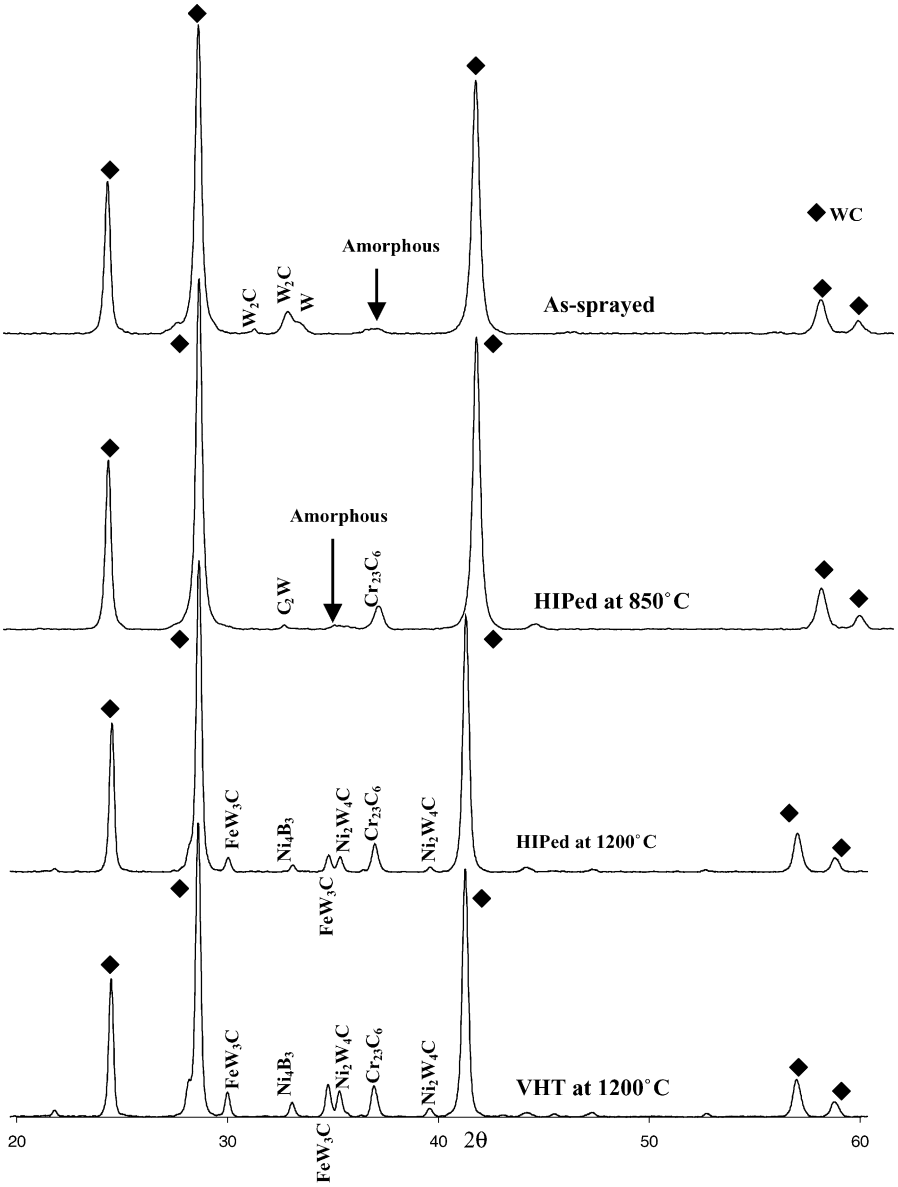

Fig. 13. XRD spectrum of the as-sprayed and post-treated coatings (WC–10% NiCr layer).

ness of the upper and lower layers were similar to the coating HIPed at 850 °C, therefore it is likely that the hardness mechanisms occurring at 850 °C were still occurring at 1200 °C. The increase in carbide dissolution and necking between the carbides led to higher elastic modulus values.

4.1.4. Vacuum heated coatings

The microstructure of the coating vacuum heated at 1200 °C was similar to HIPed at 1200 °C microstructure as shown in Fig. 11. However, a number of pores were observed within the diffusion layer, which were identified as Kirkendall pores. During HIPing at 1200 °C, these pores were closed up, however due to the absence of high isostatic pressure in vacuum heating, the pores did not reduce in size. The XRD pattern was also similar, however the narrow complex carbide peaks were slightly higher in intensity. A noticeable difference was observed in the mechanical properties of the two coatings as seen in Fig. 12(a) and (b). The hardness value for the upper layer was slightly higher than the value for the upper layer of the HIPed at 1200 °C coating, however the hardness values for the lower layer were similar. The elastic modulus of the vacuum heated coating significantly reduced with coating depth. This trend was not observed in the HIPed coatings. The increase in elastic modulus in the HIPed coatings is attributed to both carbide dissolution and necking between the carbides. Dissolution of carbides occurs at high temperatures and is not pressure dependent. The formation of chromium carbides and other phases has been observed in previous investigations on the heat treatment of WC cermet thermal spray coatings [22,23]. However, the process of necking is localised to the post-treatment, HIPing. The process of densification within the powder during HIPing at elevated temperatures is a two step process [24]. Initially, neck growth occurs at the contacts between the carbides. At this stage the carbides are beginning to bond but the porosity is still interconnected. The mechanism of this phenomena of neck growth is determined as grain boundary diffusion creep. With eventual final densification the material is considered a solid containing isolated pores. Therefore the absence of neck growth in the vacuum heated coating microstructure led to low levels of elastic modulus as observed in Fig. 12(b), which is detrimental to improvement in RCF performance.

4.2. RCF failure modes

Classification of failure modes was made on the basis of surface and sub-surface observations of the failed rolling elements. Since the modified four-ball machine runs at high speed, it is difficult to observe crack propagation. Post-test examination is the only method to ascertain failure modes and mechanisms. A principal aim of the current study was to ascertain whether similar failure modes occurred in post-treated coatings as had been previously seen in as-sprayed thermal spray coatings. Classification of failure modes in thermal spray coatings have been categorised into four main modes and named as abrasion, delamination, bulk failure and spalling [14]. However as seen in Table 1 only three modes of failure were identified in post-testing analysis. They were delamination, spalling and surface distress.

4.2.1. Delamination in RCF failure

Suh initially proposed the delamination theory of sliding wear in 1973. Suh [25], Flemming and Suh [26], Suh and Saka [27] and Suh [28] have since performed experimental and theoretical analysis supporting the delamination theory. The mechanism of delamination wear includes the propagation of cracks parallel to the surface at a depth governed by material properties and friction coefficient. Although rolling friction prevails in modified four-ball tests and delamination theory is based on sliding friction, the results are still compelling. Damage theory of materials begins with the premise that material contains a multitude of defects in the form of micro-voids [29] which undergo extension due to loading and unloading. A similar approach is adapted to explain the mechanism of coating delamination. The coating microstructure contains varying levels of micro-pores, micro-cracks and secondary phase particles, which act as stress concentration points during cyclic loading. A typical example of delamination failure on the wear track can be seen in Figs. 3(a) and (b), 4(a) and (b) and 5(a), (b) and (d).

4.2.2. Spalling in RCF failure

Spalling is the most commonly seen failure in conventional steel rolling element bearings. Spalling fatigue, however is the rarest mode of failure in thermal spray coatings. Tallian defined a spall as a sharp edged bottom feature formed by the fracture of a surface [29]. Spall in thermal spray coatings resembles in appearance to the spalls in conventional bearings and differs from delamination failure. The spall is contained within the wear track and it is circular or elliptical in appearance with its surface area (width to depth ratio) much smaller than that of a delaminated coating. Spalls can initiate from micro-pits, furrows, grinding marks or dents on the surface of a wear track. In addition, sub-surface inclusions and defects at depths of orthogonal shear stress are known to lead to spalling of rolling elements. Spalls are shown in Figs 3(d), 4(d) and 7(b).

4.2.3. Surface distress in RCF failure

Surface distress is defined as micro-scale spalling fatigue. It is the failure of rolling contact surfaces resulting in asperity scale micro-spall craters. Surface distress has been reported predominantly on steel rolling contact surfaces. However, silicon nitride ceramic components also exhibit the micro-cracking and micro-spalling features of surface distress. The theory of surface distress in metals is discussed in detail by both Tallian [29] and Suh [28]. Both define the failure process as a mechanism of asperity contact in the presence of micro-slip and sliding which is responsible for micro-pitting and sliding wear. Under full film EHL test conditions, surface distress does not occur because the film pre-

vents high micro-stresses in asperity interactions. However, if the formation of a spall or micro-pit from delamination does not trigger the vibration sensor during RCF testing, the debris from the damaged area can become trapped within the contact area which disrupts the EHL film. The damage to the coating surface is controlled by the size of the debris. The size of the debris is related to the critical crack size in the contact stress field and hence a particle cannot be crushed below this threshold. The difference in hardness between the coating and the planetary balls also has a significant effect on the material removal process. The contact is subject to micro-slip (Fig. 1) so within the contact, one surface moves with respect to the other and hence the trapped particle must accommodate this slip. As well as the mechanism of asperity deformation leading to micro-pitting of the surface, the criterion of maximum tensile stress at the edge of the contact area for brittle materials also needs to be considered. Stresses are sharply localised and decay rapidly at relatively low depths below the surface. For circular point contacts, tensile stress (T_{max}) for a given value of peak compressive stress P_0 can be evaluated from the following equation:

$$T_{max} = \tfrac{1}{3}(1 - 2v)P_0 \quad (15)$$

Tucker [30] showed that the fracture stress of WC–Co coatings using the technique of tensile test free standing ring is in the range of 380–690 MPa for high velocity plasma spray (HVPS) and detonation gun (D-Gun) coatings. The combination of high micro-hardness and the steep gradient in indentation modulus values for vacuum heated thermal spray coatings can result in low levels of fracture stress. Hence, tensile stress at the edge of the contact region under Hertzian stresses will be similar to the fracture stress. This indicates that even under the fully developed EHL regime, micro-cracks can propagate because of tensile stressing at the edge of the contact area. Figs. 3(c), 4(c), 5(c), 6(b) and (d) and 7(d) show the SEM observation of surface distress in as-sprayed and post-treated coatings.

4.3. Effect of contact stress on RCF failure modes of as-sprayed and post-treated WC–NiCrBSi coatings

4.3.1. As-sprayed coatings

Tests conducted in full film lubrication on the as-sprayed coatings highlighted the weakness in the coating microstructure, since asperity contact was prevented. Previous investigations have indicated that after significant number of stress cycles, failure can initiate within the wear track from micro-slip within the contact region which can lead to asperity contact [14]. RCF results of the as-sprayed coatings shown in Table 1 indicated that the as-sprayed coatings failed at both levels of contact stress and in full film lubrication after less than 10 million stress cycles. Mechanism of sub-surface failure in as-sprayed coatings has been classified in previous investigations as either delamination or spalling [14]. Fig. 3(a) shows delamination on the wear track of an as-sprayed coating subjected to a contact stress of 2 GPa, using steel balls in full film lubrication which endured 10 million stress cycles before failure (T01). Depth of failure was measured as 30 μm as shown in Table 2, which indicated failure initiated in the region of maximum shear stress during testing. Delamination was also observed on the wear track of the as-sprayed coating subjected to the higher contact stress of 2.7 GPa (T02) as shown in Fig. 4(a). RCF performance was lower at 1 million stress cycles however, mechanism of failure remained the same as shown by the depth of failure of 38 μm (Table 2), which was in the region of maximum shear stress.

The relative RCF performance of the as-sprayed coatings was also sensitive to the difference in hardness of the thrust ball bearings. Test T03 conducted in a hybrid ceramic bearing configuration and subjected to 2.7 GPa Hertzian contact stress displayed low resistance to rolling contact fatigue as shown in Fig. 2. Fig. 5(a) shows the mode of failure as delamination which initiated at the depth of maximum shear stress as shown in Table 2. Hence in increasing the contact pair hardness; mode and mechanism of failure remained constant.

The mechanism of failure for as-sprayed coatings was sub-surface initiated. During RCF testing, sub-surface failure initiated at the location of maximum shear stress from defects within the coating microstructure. The amorphous regions in the as-sprayed coating are brittle and hence, likely areas for crack initiation. Therefore, during RCF testing of the as-sprayed coatings, the probable mechanism of failure involved cracks initiating within these brittle regions and propagating towards the surface due to low levels of elastic modulus. This led to delamination on the wear track of the coating after relatively few stress cycles.

4.3.2. HIPed at 850 °C coatings

Previous investigations on the fatigue evaluation of coatings HIPed at 850 °C have shown little improvement in RCF performance since HIPing at this temperature resulted in a low degree of densification within the coating microstructure, and hence the mode and mechanism of failure was similar to the as-sprayed coatings [31]. Fig. 3(b) displays the delamination as the mode of failure on the wear track of a coating HIPed at 850 °C and subjected to 2 GPa contact stress in full film lubrication using steel balls which endured 8 million stress cycles (T06). Mode of failure was identified as delamination. Maximum tensile stress did not exceed the fracture stress of the coating during testing and hence, no micro-cracks were observed at the edge of the contact region. Fig. 4(b) displays the area of failure on the wear track of test T07 where a coating HIPed at 850 °C was subjected to 2.7 GPa contact stress in full film lubrication. Mode of failure was identified as delamination, however a number of cracks were observed at the edge of the delaminated area. The influence of increase in contact pair hardness resulted in lower resistance to rolling contact fatigue for coatings HIPed at 850 °C (T08) and delamination occurred on the wear track as shown in Fig 5(b).

The post-treatment of HIPing at 850 °C had no significant influence on the coating microstructure and hence no improvement in RCF performance occurred. In full film lubricated conditions, mode of failure was identified as delamination. The XRD pattern of the upper layer of the coating showed the amorphous hump, which was observed in the as-sprayed coating, and hence, did not recrystallise with HIPing at 850 °C. Therefore, it is likely that mechanism of failure was by cracks initiating in the brittle amorphous region during RCF testing at a depth of either orthogonal or maximum shear stress. The level of elastic modulus measured on the coating microstructure was not high enough to prevent crack propagation, which led to delamination failure on the wear track.

4.3.3. HIPed at 1200 °C coatings

Coatings HIPed at the elevated temperature of 1200 °C have been shown in previous investigations to display significant improvement in relative RCF performance over the as-sprayed coatings [31]. This has been attributed to carbide dissolution within the coating microstructure which prevented crack initiation at depths of either orthogonal or maximum shear stress during RCF testing. Fig. 3(c) shows the wear track of a coating HIPed at 1200 °C and subjected to 2 GPa in full film lubrication using steel balls, which endured 70 million stress cycles. The high frequency of micro-pits within the wear track was identified as the failure mode (i.e. surface distress). The formation of a dent within the wear track from an initial surface defect leads to localised thinning of the lubricant film which enables asperity interaction in the area surrounding the dent [29]. Debris from the initial asperity interaction became entrapped within the wear track during testing and hence the number of micro-pits were increased. Fig. 4(c) displays the wear track of test T12 where the coating HIPed at 1200 °C was subjected to 2.7 GPa contact stress in full film lubrication and endured 50 million stress cycles. Mode of failure was identified as surface distress. Since the coating endured a significant number of stress cycles before failing, and the mode of failure remained the same, it can be concluded that mechanism of failure remained constant with increasing contact stress. As observed in both the as-sprayed and coatings HIPed at 1200 °C, RCF performance was highly sensitive to the influence of increase in contact pair hardness. In test T13 (HIPed at 1200 °C) coating was subjected to 2.7 GPa in full film lubrication using ceramic ball bearings. As shown in Fig. 2, RCF performance was significantly reduced to 4 million stress cycles. Mode of failure shown in Fig. 5(c) was identified as surface distress although a number of micro-cracks were also observed at the edge of the contact region. The higher hardness of the ceramic balls ($HV_{300} = 1,580$) led to the micro-cracking of coating material, since the resulting increase in maximum tensile stress exceeded the fracture stress of the material.

Coatings HIPed at 1200 °C displayed improvement in RCF performance over both as-sprayed and HIPed at 850 °C coatings. In tests conducted in full film lubrication and under Hertzian stress levels of 2 GPa, improvement in RCF performance was the most significant. The mechanism of failure in the as-sprayed and HIPed at 850 °C coatings was likely to have initiated from brittle amorphous regions within the microstructure which was identified as the areas of crack initiation. As discussed in Section 4.1.3, the brittle amorphous region recrystallised to form complex carbides at the elevated HIPing temperature of 1200 °C. Crack propagation within the microstructure during RCF testing was also less likely after HIPing at 1200 °C, which was attributed to the improvement in mechanical properties. As well as an increase in elastic modulus, which indicated improved bonding between the splats; coatings heat treated at high temperatures have shown a reduction in tensile stresses and have attributed compressive stresses to the onset of cooling whereby the substrate contracts more than the coating due to thermal mismatch, which puts the coating into compression [17]. The compressive stresses prevented crack propagation within the microstructure during rolling contact. The formation of surface distress was attributed to either the possible formation of a dent within the wear track or the initiation of micro-cracks at the edge of the contact region at higher contact stresses.

4.3.4. Vacuum heated coatings

The post-treatment of vacuum heating has been shown to lead to significant densification within the coating microstructure. However, the absence of high isostatic pressing with vacuum heating results in a high gradient in elastic modulus. Hence, this increases the probability of sub-surface failure initiation [15]. Fig. 3(d) shows the area of failure on the wear track of a vacuum heated coating subjected to 2 GPa in full film lubrication using steel balls which endured 70 million stress cycles (T16). Mode of failure was identified as spalling. Depth of failure was measured as 31 μm which was in the region of orthogonal shear stress. Hence failure was sub-surface initiated since sub-surface spalling initiates at depths above the location of maximum shear stress during RCF testing [29]. Mode of failure was identified as spalling in T17 where the vacuum heated coating was subjected to 2.7 GPa and endured 2 million stress cycles as shown in Fig. 4(d). Depth of failure was in the region of orthogonal shear stress indicating failure was sub-surface initiated. The influence of increasing contact pair hardness reduced the RCF performance of vacuum heated coatings. Fig. 5(d) displays the area of failure on the wear track of a vacuum heated coating subjected to 2.7 GPa contact stress which endured 1 million stress cycles (T18). Mode of failure was identified as delamination. Depth of failure was less than the depth of orthogonal and maximum shear stress. With the increase in contact pair hardness as well as the high gradient in elastic modulus results, it is likely that the failure occurred due to crack initiation at the edge of the rolling contact region during testing. Propagation of the cracks led to sheet like debris delaminating from the wear track.

The mechanism and modes of failure highlighted the important influence of isostatic pressure during post-treatment on the performance of thermal spray coatings in rolling contact fatigue testing. In tests conducted using full film lubrication, vacuum heated coatings displayed improved performance over the as-sprayed coatings at Hertzian contact stress of 2 GPa. At higher levels of Hertzian contact stress, the relative RCF performance was significantly reduced. The observation of sub-surface spalling in test T17 was attributed to the significant reduction in indentation modulus. Hence, it can be concluded that the influence of high isostatic pressure during post-treatment led to improved bonding between the splats, which prevented sub-surface cracks propagating within the microstructure of HIPed coatings.

4.4. Influence of lubrication regime

RCF tests were also conducted in the mixed regime ($1.5 < \lambda < 3$) using Exxon lubricant where surface asperities came into contact. Williams [16] has shown that under mixed film regime, the asperity contact and EHL film share the load. According to Berthe et al. [32] these asperity contacts produce high stress concentrations very close to the surface but do not change the sub-surface Hertzian stress pattern. These stress concentrations which are due to the interaction of asperities in the presence of micro-slip within the contact region result in a shear stress beneath the asperities. Hard coatings such as WC–Co respond by micro-cracking.

4.4.1. As-sprayed coatings

Previous RCF investigations on as-sprayed coatings in the mixed regime have concluded that the main mode of failure was surface distress. A combination of factors such as asperity contact and tensile stress at the edge of the contact region, coupled with micro-slip sliding within the contact region generated initial wear debris in two body abrasion. They were reported as the main mechanisms of failure controlling the rate of abrasion [13]. Fig. 6(a) shows the area of failure on the wear track of an as-sprayed coating subjected to 2 GPa contact stress on mixed film regime which endured 7 million stress cycles (T04). A number of micro-cracks have formed at the edge of the contact region due to asperity interaction in the contact region. Fig. 7(a) displays the area of failure on the wear track of an as-sprayed coating which was subjected to a higher Hertzian contact stress of 2.7 GPa in mixed film regime which endured 1 million stress cycles (T05). The influence of increase in contact stress raised the maximum tensile stress during testing. This resulted in lower resistance to rolling contact fatigue and coating delaminating from the wear track.

4.4.2. HIPed at 850 °C coatings

Coatings HIPed at 850 °C displayed higher values of micro-hardness and elastic modulus. Increase in elastic modulus indicated improved bonding between the splats, which may increase the fracture strength of the coating. This can lead to improved performance in RCF tests. Fig. 6(b) shows the area of failure on the wear track of a coating HIPed at 850 °C and subjected to 2 GPa which endured 9 million stress cycles (T09). A number of micro-cracks were observed at the edge of the contact region, hence mechanism of failure was similar to as-sprayed coatings. However, as shown in Fig. 2, the relative RCF performance was slightly higher. Mode and mechanism and failure remained constant in the test conducted on HIPed at 850 °C coating subjected to the higher contact stress of 2.7 GPa as shown in Fig. 7(b). RCF performance was lower in test T10 as shown in Fig. 2, since increase in contact stress led to higher levels of maximum tensile stress during testing, which increased the rate of crack initiation at the edge of the contact region.

4.4.3. HIPed at 1200 °C coatings

HIPing at elevated temperatures increased the micro-hardness and elastic modulus of the coating layer as shown in Fig. 12, which resulted in relatively improved RCF performance. Fig. 6(c) displays the area of failure on the wear track of a coating HIPed at the elevated temperature of 1200 °C and subjected to 2 GPa in mixed film regime, which endured 20 million stress cycles (T14). Macro-cracks were observed at the edge of the contact region indicating a similar mode and mechanism of failure to what was observed for other tests conducted with HIPed at 1200 °C coatings. The improvement in coating microstructure was attributed to the significant improvement in relative RCF performance as shown in Fig. 2. Fig. 7(c) shows the area of failure on the wear track of the HIPed at 1200 °C coating subjected to 2.7 GPa contact stress in mixed film regime (T15). The increase in contact stress resulted in coating delaminating from the wear track. Although no micro-cracks were observed it is likely mechanism of failure was surface initiated since micro-cracks were observed at the lower contact stress of 2 GPa.

4.4.4. Vacuum heated coatings

Previous investigations on vacuum heated coatings have shown that this method of heat treatment causes changes in the residual stress state of the coating and its integrity because of thermal expansion mismatch between the coating and substrate. This led to a reduction in tensile stress and produced coating cracking. Micro-cracking and reduction in residual stresses was seen as beneficial in promoting abrasive wear resistance of post-treated thermal spray coatings, since micro-cracking within the coating microstructure diverted deep sub-surface cracks and prevented them from propagating, while low residual stresses also reduce the tendency for cracks to propagate [9]. Indentation measurements on vacuum heated coatings, as shown in Fig. 12(b), were extremely high on the surface but dropped at a high gradient in moving into the microstructure, which indicated a lack of homogeneous behaviour. Fig. 6(d) shows the area of failure on the wear track of a vacuum heated coating subjected to 2 GPa contact stress in mixed film regime using steel ball

bearings, which endured 2 million stress cycles. Mode of failure was identified as surface distress and delamination, since width of failure was significantly greater than the contact width listed in Table 1. Depth of failure was measured as 33 μm. In test T20, a vacuum heated coating was subjected to the higher Hertzian contact stress of 2.7 GPa in mixed film regime, which endured 2 million stress cycles. Mode of failure was identified as surface distress, which formed from propagation of micro-cracks at the edge of the contact region as shown in Fig. 7(d).

5. Three ball set-up versus thrust bearing set-up

Prior to this investigation, post-treated functional graded thermal spray coatings were tested in a modified four-ball rolling contact fatigue machine in a three ball and disc configuration [11]. Results showed superior performance of coatings HIPed at the elevated temperature of 1200 °C over the as-sprayed coatings when subjected to a Hertzian contact stress of 2 GPa in full film lubrication. However, for the tests conducted at a higher Hertzian contact stress of 2.3 and 2.7 GPa, the relative improvement in RCF performance was less apparent. Analysis of the failure modes and mechanisms indicated that the coating was delaminating from the wear track, which was a result of gross sliding within the contact region during RCF testing, and led to asperity interaction between the surface of the coated disc and the lower planetary balls.

In the current investigation, a thrust bearing replaced the three lower planetary balls during the rolling contact fatigue tests. The ball bearings rolled along a closely conforming groove, hence the idealizations of non-conforming contacts were no longer strictly tenable. Therefore, the amount of slip occurring in the system was significantly reduced. RCF test results in the current investigation showed relative improvement in the performance of coatings HIPed at 1200 °C over the as-sprayed coatings when subjected to the Hertzian contact stress of 2 GPa in full film lubrication. Coated discs HIPed at 1200 °C also displayed significant improvement in RCF performance over as-sprayed coatings at the higher Hertzian contact stress of 2.7 GPa. This behaviour was not observed in the previous investigation, in which HIPed at 1200 °C discs endured only 10 million stress cycles before failure occurred. In contrast, the HIPed at 1200 °C disc endured 50 million stress cycles without failure in the current investigation. The improvement in RCF performance was attributed to a reduction in sliding within the contact region in the current RCF configuration.

6. Conclusions

HIPing at elevated temperatures of 1200 °C resulted in significant improvement in relative RCF performance at all levels of contact stress in full film lubrication using steel balls. Improvement in RCF performance at the higher Hertzian contact stress of 2.7 GPa was attributed to significant improvement in the coating microstructure. The high temperatures of HIPing led to the formation of a number of new complex carbides which increased the coating hardness while high isostatic pressure improved bonding between the splats, which improved the elastic modulus of the coating. The influence of contact pair hardness (ceramic balls) increased maximum tensile stress within the contact region during RCF testing, which resulted in failure by surface delamination form micro cracking at the edge of the contact region. A change in failure mode from delamination and spalling to surface distress was observed on the wear tracks of the HIPed at 1200 °C coatings. The absence of sub-surface failure highlighted the potential improvement coatings HIPed at 1200 °C can bring to high stress tribological applications, however further testing is inevitable to ascertain the optimal tribological conditions in which these post-treated coatings can withstand high stresses, without showing evidence of surface failure.

Coatings vacuum heated at 1200 °C displayed improved performance in RCF tests conducted in full film lubricant and at 2 GPa contact stress. This post-treatment also led to the formation of complex carbides. However, the absence of high isostatic pressure in the post-treatment resulted in a lack of homogeneous behaviour (in terms of its mechanical properties) within the coating microstructure. Therefore, at higher levels of contact stress, cracks initiated at depths of orthogonal shear stress which resulted in spalling. Increase in contact pair hardness during RCF tests led to the initiation of micro-cracks at the edge of the contact region, which was attributed to levels of maximum tensile stress evaluated from extremely high indentation modulus values measured on the surface.

Coatings HIPed at 850 °C showed no improvement in performance over the as-sprayed coatings in RCF testing. However, the influence of high isostatic pressure improved bonding between the splats. HIPing at the lower temperature of 850 °C led to the formation of complex carbide phases which improved coating hardness, however, the amorphous region observed in the spectrum of the as-sprayed coating remained. During RCF testing it is likely that the cracks initiated within this brittle amorphous region, which propagated and resulted in coating delamination.

Acknowledgements

The authors would like to thank Dr. Susan Davies at Bodycote Hot Isostatic Pressing Ltd/Infutec Ltd. for post-treatment of thermal spray coatings, and also Professor Rainer Gadow at the University of Stuttgart for the indentation modulus measurements. The authors also acknowledge the financial support by the Engineering and Physical Sciences Research Council (EPSRC-GR/R45284).

References

[1] A. Nakajima, T. Mawatari, M. Yoshida, K. Tani, A. Nakahira, Effects of coating thickness and slip ratio on the durability of thermally sprayed WC cermet coatings in rolling/sliding contact, Wear 241 (2000) 166–173.

[2] J. Birch, M. Koizumi, T. Hirai, in: Proceedings of the Second International Symposium on Functionally Gradient Materials, 34, The American Ceramic Society, Ceramic Transactions, San Francisco, 1992.

[3] B. Ilschner, in: Proceedings of the Third International Symposium on Structural and Functionally Gradient Materials, Lausanne, 1994.

[4] W.A. Kaysser, Functionally Graded Materials, Dresden, 1998, Materials Science Forum, 1999, pp. 308–311.

[5] S. Suresh, A. Mortensen, Fundamentals of Functionally Gradient Materials, The Institute of Materials, University Press, Cambridge, 1999.

[6] F. Voort, A Layman's view of plasma spray coating metallography, Structure 28 (1995) 8–13.

[7] R.W. Smith, R. Novak, Advances and application in US thermal spray technology, Powder Metall. Int. 23 (1991) 147–156.

[8] H.D. Steffens, K. Nassenstein, Thermal spraying: a review of 1993, Powder Metall. Int. 25 (1993) 280–284.

[9] D.A. Stewart, P.H. Shipway, D.G. McCartney, Influence of heat treatment on the abrasive wear behaviour of HVOF sprayed WC–Co coatings, Surf. Coat. Technol. 105 (1998) 13–24.

[10] H.C. Chen, E. Pfender, J. Heberlein, Structural changes in the plasma sprayed ZrO_2coatings after hot isostatic pressing, Thin Solid Films 293 (1997) 227–235.

[11] S. Stewart, R. Ahmed, T. Itsukaichi, Rolling contact fatigue of post-treated WC–NiCrBSi thermal spray coatings, Surf. Coat. Technol., 2003, submitted for publication.

[12] J. Nerz, B. Kushner, A. Rotolico, Microstructural evaluation of WC–Co coatings, J. Therm. Spray Technol. 11 (2) (2002) 1–17.

[13] R. Tourret, E.P. Wright, Rolling contact fatigue: performance testing of lubricants, in: Proceedings of the International Symposium on Petroleum, Heydon, London, 1977.

[14] R. Ahmed, M. Hadfield, Mechanisms of fatigue failure in thermal spray coatings, J. Therm. Spray Technol. 11 (2) (2002) 1–17.

[15] R. Ahmed, M. Hadfield, Rolling contact fatigue performance of plasma sprayed coatings, Wear 220 (1998) 80–91.

[16] J.A. Williams, Engineering Tribology, Oxford University Press, Oxford, 1994.

[17] H.L. de Villiers Lovelock, Powder/processing/structure relationships in WC–Co thermal spray coatings: a review of the published literature, J. Therm. Spray Technol. 7 (3) (1998) 357–363.

[18] C.J. Li, A. Ohmori, Y. Harada, Formation of an amorphous phase in thermally sprayed WC–Co, J. Therm. Spray Technol. 5 (1996) 69–73.

[19] H.C. Lee, J. Gurland, Hardness and deformation of cemented tungsten carbide, Mater. Sci. Eng. 33 (1978) 125–133.

[20] J. Gurland, Application of quantitive microscopy to cemented carbides, in: Practical Applications of Quantitive Metallography, American Society for Testing and Materials, Philadelphia, 1984, pp. 65–84.

[21] T. Tomita, et al., Mechanisms of High Hardness in Cr_3C_2–NiCr Cermet Coatings Formed by Vacuum Plasma Spraying, Thermal Spray 2001: New Surfaces for a New Millennium, ASM International, Materials Park, OH, USA, 2001, pp. 699–704.

[22] R. Okada, M. Yamanda, Effect of heat treatment on hardness and wear resistance of WC–NiCr sprayed coatings, Jpn. Inst. Met. 58 (7) (1994) 763–767.

[23] D. Zhang, M. Kato, K. Nakasa, K. Tasaka, Effect of heating in air or in a vacuum on the delamination strength of WC–Co coating deposited by high velocity flame spraying, J. Soc. Mater. Sci. Jpn. 48 (9) (1999) 1065–1071.

[24] J.J. Conway, B.A. Hann, Hot isostatic pressing of metal powders: a commercial success, ASME 384 (1999) 91–99.

[25] N.P. Suh, An overview of the delamination theory of wear, Wear 44 (1997) 1–16.

[26] J.W. Flemming, N.P. Suh, Mechanics of crack propagation in delamination wear, Wear 44 (1977) 39–56.

[27] N.P. Suh, N. Saka, Fundamentals of tribology, in: Proceedings of the International Conference on the Fundamentals of Tribology, MIT Press, 1980.

[28] N.P. Suh, Tribophysics, Prentice-Hall, New York, 1986.

[29] T.E. Tallian, Failure atlas for Hertz contact machine elements, ASME, 1999.

[30] R.C. Tucker Jr., Structure and property relationship in deposits produced by plasma spray and detonation gun techniques, J. Vac. Sci. Technol. 11 (1994) 725–734.

[31] S. Stewart, R. Ahmed, Contact fatigue failure modes in hot isostatically pressed WC–12% Co coatings, Surf. Coat. Technol. 172 (2003) 204–216.

[32] D. Berthe, L. Flamand, M. Godet, Micropitting in Hertzian contacts, J. Lubr. Technol. 102 (1980) 479–485.